HELLENIC REPUBLIC
National and Kapodistrian University of Athens
EST. 1837

School of Health Sciences

Faculty of Medicine

and

Faculty of Pharmacy

Interdisciplinary M.Sc. course in Nanomedicine

Academic year 2021-2022

Hybrid materials for biomedical applications

M.Sc Student : Ioanna – Aglaia D. Vagena

SCIENTIFIC COMMITTEE

Nefeli Lagopati , Assistant Professor , NKUA

Efstathios Efstathopoulos , Professor , NKUA

Maria Gazouli , Professor , NKUA

Athens

August 2022

Acknowledgments

I would like to express my deepest gratitude to my supervisor, professor Nefeli Lagopati for her trust and belief in me from the day one and her continuous guidance with her expertise during the last one year, as well as the other two members of the scientific committee, professor Efstathios Efstathopoulos and professor Maria Gazouli for their knowledge and invaluable feedback.

Also, I would want to extend my sincere thanks to the PhD candidates of the National Technical University of Athens, General Chemistry Laboratory, School of Chemical Engineering, Ms. Marianna Gatou and Mr. Dimitris Manousakis for their daily guidance and support at the experimental part of my thesis, people without whom my project would be impossible.

Lastly, I am grateful to my family and friends who helped me to grow along the way with their patience, emotional support, and encouragement, people who have highly contributed on who I have been and what I have been learning and offering so far.

Table of Contents

Table of Abbreviations

PDT	Photodynamic Therapy
ROS	Reactive Oxygen Species
EPR	Enhanced permeability and retention
NPs	Nanoparticles
ZnO	Zinc Oxide
CQDs	Carbon Quantum Dots
UV	Ultraviolet
UV-Vis	Ultraviolet-Visible
SPT	Single particle tracking
DOX	Doxorubicin
MRI	Magnetic Resonance Imaging
rRNa	ribosomal RNA
PA	Photoacoustic Imaging
PL	Photoluminescence
LA	Longitudinal acoustic
TA	Transverse acoustic
LO	Longitudinal acoustic
TO	Transverse optical
PET/CT	Positron emission tomography/computed tomography
MTAP	Meso-tetra o-amino phenyl porphyrin
PACT	Photodynamic antimicrobial chemotherapy
DLS	Dynamic Light Scattering
XRD	X-Ray Diffraction
FTIR	Fourier- Transformed Infrared (FTIR)
DTGS	Deuterated Triglycine Sulfate
SNR	Signal-to-Noise Ratio
MDA-MB-231	Human epithelial breast adenocarcinoma
DMEM	Dulbecco's modified Eagle's medium
FBS	Fetal Bovine Serum
MCF-7	Epithelial breast adenocarcinoma
A549	Human epithelial lung carcinoma
HEK293	Normal human epithelial kidney embryonic cells
EDTA	Trypsin–Ethylenediaminetetraacetic acid
DMSO	Dimethyl Sulfoxide

Abstract

Cancer is a worldwide cause of death and new ways of imaging and therapy are being discovered. A new hybrid material was proposed consisted of carbon quantum dots, ZnO and porphyrin, intended to be a theranostic material. Carbon quantum dots electrochemical process is a low cost and innovative method. CQDs excellent fluorescence properties make them promising material for molecular imaging. Porphyrin's derivatives have the potential to be employed in Photodynamic therapy. ZnO nanoparticles due to their enhanced permeability and retention effect have the potential to become a promising anticancer effect. The toxicity of CQDs, porphyrin and Zno was tested by MTT colorimetric assay in normal cell lines HEK231 and cancer cell lines A549, MCF-7 and MDA-MB-231.

1. Introduction

Cancer is a multifactorial disease characterized by alterations in cell processes that cause cells to become overactive, increase in growth and proliferation rate, aggressive, invading and destroying nearby tissues and metastatic, since they can migrate to other organs [1] . The scientific community approaches cancer sickness in a variety of ways, but there are still areas of study field of alternative cancer treatments that have yet to be found, with an emphasis on minimazing the negative repercussions of standard treatment methods [2]. Radiation therapy, chemotherapy and immunotherapy, alone or in combination, are essential components of numerous cancer treatment strategies for effective multimodal conventional cancer management. Nanoparticles have considerable potential in photodynamic therapy because they have the ability to stimulate the production of reactive oxygen species (ROS) when exposed to light (PDT). PDT is a medically used treatment technique, also known as phototherapy, photoradiation therapy, or photochemotherapy [3].PDT is most commonly wont to treat malignant neoplasm cells, sun broken skin, acne, rosacea , onychomicosis, and other inflammatory illnesses and cutaneous infections. It is also used in PDT in a style of growth diseases, together with epithelial cell malignant neoplastic disease, actinic keratoses, basal cell malignant neoplastic disease and utaneous T cell lymphoma [4]. PDT requires 3 components: a photosensitizer (PS), a light-weight supply and oxygen. The photosensitizing agent is a chemical that binds to the target sell or tissue and might be activated by light-weight within the presence of chemical element [5]. When exposed to specified wavelengths, the photosensitizer transitions from the “ground state” to the “excited state”. Returning to the starting state, energy is released in two ways, allowing selective cytotoxicity to occur. It can react with the substrate, producing reactive oxygen species (ROS) that can oxidize important biological components, resulting in apoptosis or necrosis. Alternatively, the energy is often transferred to chemical elements, resulting in an undershirt chemical element which subsequently oxidizes diverse substrates, thereby mediating the selective killing effect. Controlling the duration and depth of the irradiation will facilitate to scale back the harm to adjacent healthy tissue [6]. Porphyrin is a typical photosensitizing compound that is

mostly found in mitochondria and causes programmed cell death when exposed to light.[8] In clinical practice, the photosensitizer is applied topically, followed by an "occlusion time" that allows the medication to be digestible and accumulate porphyrins before light-weight activation. Finally, the photosensitivity required for this treatment is provided by the porphyrins created [3]. To provide a therapeutic impact, the spectrum output of the light source could be related to the excitation peaks of the chosen photosensitizer, depending on the application. Thus, the next generation of PDT can be strengthened by using nanotechnology-based drug delivery methods to harness the visible range of the electromagnetic spectrum. ZnO nanoparticles (NPs) can allow precise targeting of tumor tissues while reducing PS accumulation in healthy tissues and eliminating negative side effects. The nanoparticles can increase the retention period in the malignant tissue by improving its permeability and retention (EPR effect). The drug-light interval is thus improved, giving clinicians a larger window of time for irradiation [7]. ZnO NPs are a promising anticancer agent due to their distinctive qualities like biocompatibility, high specificity, raised cytotoxicity, and simple manufacturing. Zinc, being one among the foremost verdant trace components within the human body and a cofactor for over 300 mammalian enzymes, is essential for the maintenance of critical cellular functions like oxidative stress, deoxyribonucleic acid replication and repair, cell cycle progression and programmed cell death [8]. As a result, it is obvious that changes in zinc levels in cancer cells might have a negative impact. According to research, low zinc concentration in cells promotes cancer development and progression, while high zinc concentration causes toxicity. The likely mechanism of this harmful action is zinc-mediated macromolecule activity imbalance and oxidative stress via reactive oxygen species (ROS). The selective localization of ZnO NPs towards cancer cells because of enhanced permeability and retention (EPR) effect and electrostatic interaction, still as selective toxicity because of increased ROS levels in cancer cells, demonstrate that ZnO NPs can target and kill cancer cells, making them a promising antitumor agent [8]. Carbon quantum dots (CQDs) with a diameter of less than ten nm have attracted appreciable interest because of their sensible biocompatibility, sensible cell porousness, low toxicity, great dispersibility in water, flexibility in surface modification, chemical immobility and sensible optical performance, thus it

is new kind of fluorescent material for molecular imaging [9]. CQDs are therefore seen as the next generation of green nanomaterials, potentially contributing to a large varies of promising applications such as photoelectrocatalysis, targeted drugs delivery, electrical devices, sensing and bioimaging [10].

The aim of this study is the development of a hybrid material with photo-induced visible light anticancer properties, related to cytotoxicity. This hybrid material consists of CQDs, ZnO and pophyrin. This combination could ideally lead to the creation of a hybrid material for imaging and therapy.

2. Conceptual Framework

2.1 Carbon Quantum Dots

CQDs have piqued the interest of many global researchers within the recent years, owing to their distinctive qualities like tiny size, great biocompatibility and photo-stability, photoluminescence properties and simple pathways of functionalization [11, 12]. Clusters are typically 10 nm in size, while 5 nm is preferable for some applications [11]. Xu's et al inadvertent finding of CQDs during the separation and purification of single-walled carbon nanotubes in 2004 sparked subsequent research to leverage CQD fluorescence features and produce a new category of sensible fluorescent nanomaterials [11, 13]. The top-down route and the bottom-up route are wont to synthesize CQDs utilizing chemical, electrochemical, or physical methods.

2.1.1 "Top-Down" Method

CQDs top-down synthesis methods include the degradation of carbon compounds such as graphite, for example. CQDs production is dependent on the breakdown of bonds between carbon atom [14]. Electrochemical method, ultrasonication treatment and laser ablation are among the most important top-down synthesis methods.

- Electrochemical method: An example of an electrochemical method is the use of graphite rods as both anode and cathode electrons, while the electrolytic solution was the NaOH/ethanol combination [15]. (Figure 2.1)

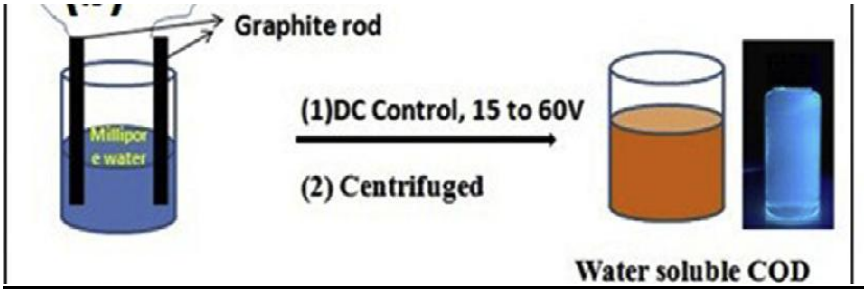

Figure 2.1: CQD synthesis by electrochemical method (Adapted by Das, R., Bandyopadhyay, R., & Pramanik, P. (2018). Carbon quantum dots from natural resource: A review. Materials Today Chemistry, 8, 96–109.)

- Ultrasonication treatment: The CQDs method by ultrasound processing is especially easy, in which carbon compounds are broken with the help of high-energy ultrasonic vibrations.
- Laser ablation: In this method, a high energy pulse is used to irradiate a solid graphitic target that is in a liquid or gaseous environment [16].

2.1.2 "Bottom-up" Method

CQDs bottom-up synthesis methods include tiny organic molecule pyrolysis or carbonization [14]. Some of the most important bottom-up synthesis methods are:

- Hydrothermal method: The hydrothermal method is any heterogeneous chemical reaction carried out in a closed system in the presence of an aqueous or non-aqueous solvent. Temperatures rise above room temperature, while pressure rises above atmospheric levels. It is a simple and inexpensive procedure. Citric acid, glucose etc. are employed as carbon precursors. In a self-healing container, an aqueous or non-aqueous solution of the precursor compound is sealed [14] (Figure 2.2).

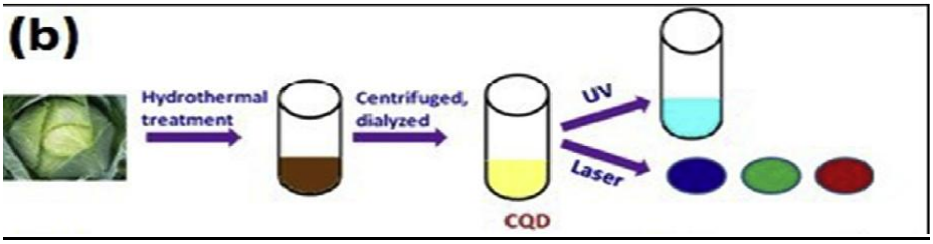

Figure 2.2: Synthesis of CQD from cabbage ((Adapted by Das, R., Bandyopadhyay, R., & Pramanik, P. (2018). Carbon quantum dots from natural resource: A review. Materials Today Chemistry, 8, 96–109.)

- Microwave-Assisted hydrothermal method: Microwave radiation can be used to perform the hydrothermal process. With energy savings, a shorter reaction time is necessary [14].

2.1.3 Doping of CQDs

The primary aim for doping in CQDs is to achieve a straightforward and simple technique for introducing sites of higher activity to increase foundational features through heteroatom's electron lone pairs. Dopants can be either metallic or nonmetallic, and they can improve fluorescence by changing the band gap and introducing new energy levels [17]. Nonmetallic dopants decrease the energy gap between orbital and carbon's orbital which does not bond and by this way quantum yield increases. Metallic dopants, on the other hand, chelating to utilitarian bunches in forerunners amid carbonizationor lack of hydration to alter band structure [18]. The doping mechanism is defined by the quantity of dopants and their bonding orientations [17]. Doping with N atoms has been proved as the approach of highest efficiency, while nitrogen, which is next to carbon and has 5 e^- in valence band embedded into the structure of carbon quantum dots by replacing carbon. Nitrogen-bound CQD surfaces come in a variety of configurations, including graphitic, pyridinic, and pyrrolic forms, each with its own electron transport capabilities [19-21]. The amount of dopant has a positive correlation with fluorescence behavior. CQDs doping has proven to be an effective approach for producing singlet oxygen, which is essential in photodynamic therapy (PDT) [22].

2.1.4 Fluorescence properties of CQDs

Although the genuine beginnings of CQDs fluorescence outflows are obscure, two sorts of fluorescence outflow instruments have been hypothesized, and extra investigate is needed to create a fuller image of the instruments of their unmistakable light outflows. The first kind of visible radiation emissions method contains bandgap changes produced by conjugated π-domains, though the moment sort has more complicated sources related with surface recognizes in CQDs. Bandgap moves result from conjugated π-domains in the first one. These π-domains area unit confined by shaping sp2 hybridized islands wealthy in π- These π-domains square measure isolated by forming sp2 hybridized islands wealthy in π electrons ,reducing graphene oxides generated by oxidizing and exfoliating atomic number 6 flakes victimization Hummer's technique. There are not any π –connections between the sp2 islands, since these would result in inter island dampening of desirable fluorescence emissions [19-24]. To avoid interlayer extinguishing, single layer graphene, single-layer graphene sheets should be used at these bandgap transitions. The single-layer graphene sheets work as forerunners for electronically cutting into confined π-conjugated spaces that imitate gigantic fragrant particles with expanded π-conjugation of worthy electronic vitality bandgaps for optical retention and fluorescence outflows. This kind of electronic moves exhibit substantial ultraviolet (UV) absorption, however weak or no visible light emissions [25].

The second type of fluorescence mechanism is caused by surface-related faulty sites; in general, any site with non perfect sp2 domains can lead to energy surface traps. CQDs contain each sp2 and sp3 hybridized carbons, in addition as extra functionalized surface, which contribute to their coloured emissions, that area united targeted within the blue and inexperienced components of the light spectrum [26, 27]. Since of the nearness of numerous surface abandons with variable excitation and outflow properties, these surface appear multicolor outflows (Figure 2.3) [25]. The brilliant surface fluorescence of CQDs is caused by electron-hole combine recombination within the powerfully localized levels of the sp2 sites. These

sites area unit set between the bandgaps of the σ and σ* states of the sp3 matrix, lead to intense visual outflows. These moves have minimal absorption inside the near to ultraviolet –visible (UV-vis) region however high emissions in the high range [28].

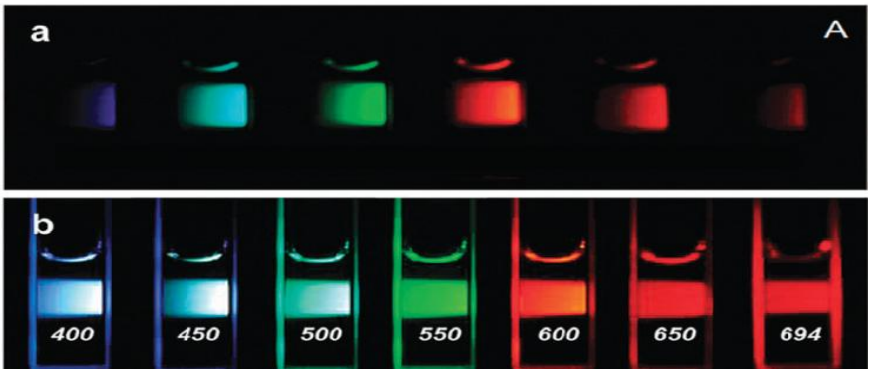

Figure 2.3: Aqueous solutions of PEG1500N-passivated CQDs (a) excited at 400 nm and (b) excited at the indicated wavelengths [15]

2.1.5 Biomedical Applications of CQDs

Biomonitoring

The real–time dynamic observation of biomolecules in living cells will shed light on a variety of enigmatic events in cell biology, such as molecule translocation, interaction with partners, and environmental signal response [11]. Single particle tracking (SPT) is a technology that allows for the high-resolution tracking of single biomolecules. Actual molecule motions can be tracked by utilizing brighter probes, such as semiconductor QDs in SPT. Chemical composition, shape, size and surface changes all have an impact on the photophysical features of semiconductor QDs [29, 30].

i) Cell imaging *in vitro*

CQDs are easily taken up by cells and permitted for cell imaging via each single and multiple gauge boson excitations [38]. Bhunia et al. described how chemically

produced CQDs were used for biological labeling and imaging. TAT peptide or folate functionalized CQDs were combined with cell culture medium and examined with fluorescence microscope after several hours of incubation. The CQDs have color-controlled emissions in blue, green, and red [23, 31]. CQDs can potentially be employed in drug delivery systems for multifunctional fluorescence imaging/magnetic resonance imaging (MRI). For instance, with the help of an 808 nm laser, Fe3O4/CQDs coated CNTs were employed for photodynamic and photothermal therapy (PTT). The platform was conjointly loaded with doxorubicin (DOX) for use in medication delivery. A sgc8c aptamer was conjugated to the platform. The nanovehicle that developed was employed for targeted light imaging/MRI. When the nanovehicle was incubated with carcinoma cells so exposed to laser light-weight, it had been ready to kill the bulk of the cancer cells. This occurrence was ascribed to the production of OH and O2, as well as the simultaneous release of DOX and formation of heat [32].

ii) Cell imaging *in vivo*

High fluorescence intensity, biocompatibility, and nontoxicity are the primary prerequisites for using nanomaterials for in vivo bioimaging. Because of their outstanding fluorescence characteristics and lack of cytotoxicity, CQDs can be employed for *in vivo* cell imaging [33]. Longer wavelengths are preferable for *in vivo* imaging due to increased photon tissue penetration. As seen in figure 2.4, the fluorescence emission of CQDs is weaker at longer wavelengths. However, for longer wavelength excitations (red and NIR), signal-to-noise ratios increase thanks to a reduction in tissue auto-fluorescence background. In fact, longer wavelengths are recommended for in vivo imaging due to photon tissue penetration and less background autofluorescence [34]. CQDs can also be employed for nucleus imaging. The organelle is that the cell's ribosomal RNA (rRNA) producing location and ribosome works. It was demonstrated that CQDs can be employed for fastened cell nucleolus imaging as well as trailing of living cell nucleolus –related behaviors. After cellular internalization, CQDs migrate rapidly toward the nucleus after 5 minutes of incubation and remain localized at nucleoli even after 24 hours. This suggests that CQDs are often utilized as dyes in nuclear fluorescence imaging [35].

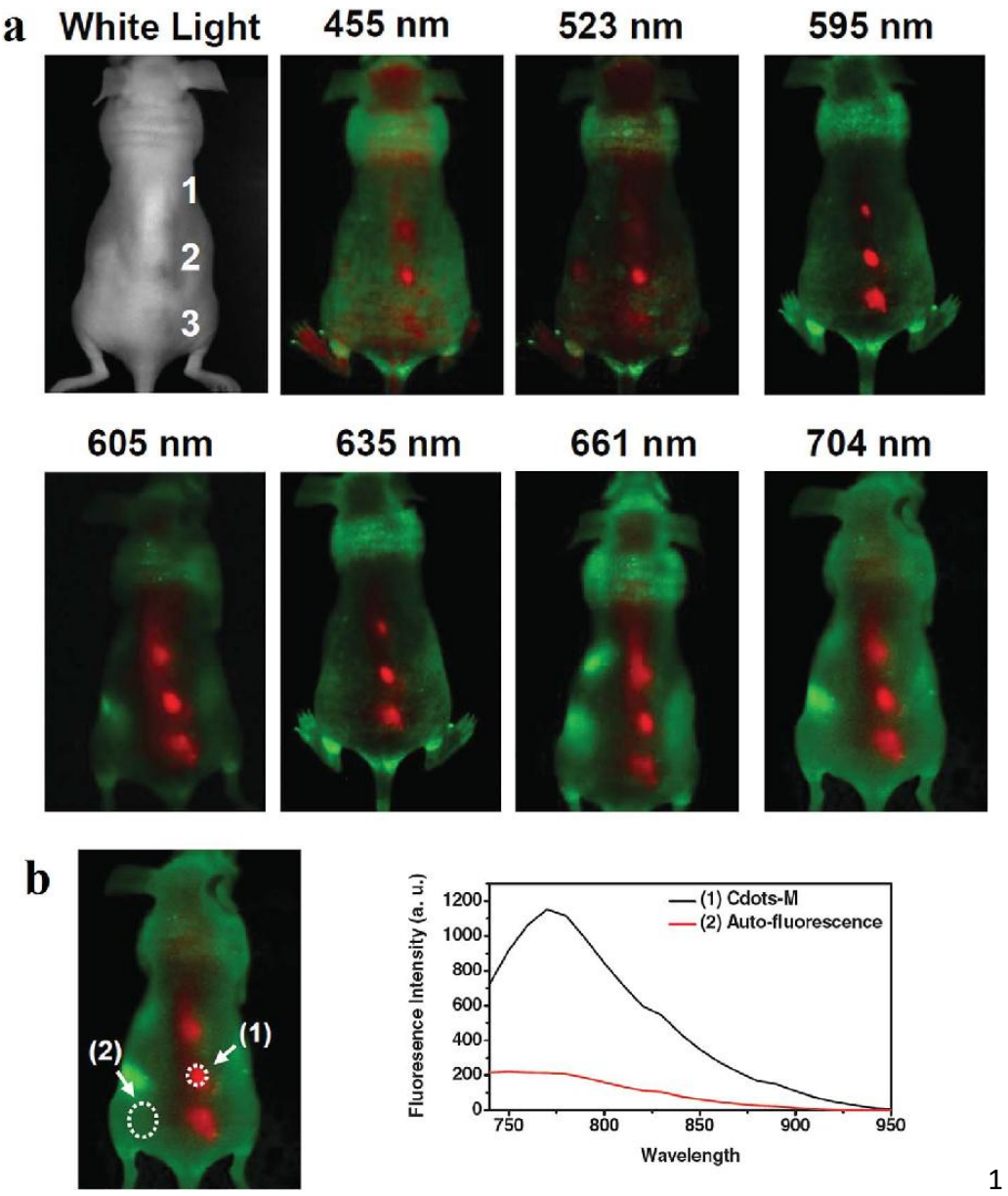

1

Figure 2.4 :(a) The in vivo fluorescence images of CQDs that are injected into a nude mouse; the excitation wavelengths are indicated above each image. The fluorescence signal and tissue autofluorescence can be seen in red and green emissions, respectively. (b) Signal-to-background separation of the image taken under 704 nm excitation [11]

Photoacoustic imaging

PA imaging combines optical excitation with ultrasonic detection, permitting imaging past the limits of optical imaging dissemination. As a result, combining fluorescence and PA imaging in a very single probe may leads in more profound tissue entrance

with fabulous imaging affectability. Ultrasonically, dispersion is eliminated, allowing for centimeter-depth penetration with increased spatial resolution. Further, PA can produce high-resolution structural images of the tumor, and fluorescence imaging will provide tumor accuracy by molecular probing [11, 36, 37].

2.2 ZnO Nanoparticles

2.2.1 Properties of ZnO

At ambient temperature, Zno has a significant exciton binding energy of 60 meV and is a semiconductor [38, 39]. Using nanoscale ZnO can potentially affect its features and, more specifically, it can influence its electrical, optical and magnetic properties [40, 41]. ZnO is a safe material because it is consistent with living organisms, making it appropriate for daily applications that pose no dangers to human health or the environment [41]. ZnO has garnered a lot of attention for its role in the breakdown and mineralization of environmental contaminants [42-44]. The ability of ZnO to soak up a wider vary of solar spectrum and a lot of light-weight quanta than some semiconductive metal oxides is its most significant benefit [45]. The main disadvantages of ZnO are its high band gap energy and photocorrosion. ZnO's light-weight is restricted within the light space as a result of its broad band energy. This causes rapid recombination of photogenerated charges, resulting in low photocatalytic potency [46].

2.2.2 ZnO structure

ZnO has explicit crystal forms, with the majority of them being rocksalt, wurtzite or cubic. Under high pressure, a rocksalt structure of ZnO can be formed, making ZnO in this structure quite unusual. The thermodynamic stability of the ZnO wurtzite structure is the most noteworthy of the three setups . At room temperature and pressure, Zno contains a hexangular wurtzite crystal structure severally [47]. This ZnO polygon house cluster structure has a place to the P63mc house gather and incorporates a non-centrosymetric structure, making ZnO piezoelectric and

pyeroelectric [48]. A no symmetric ZnO structure is the absence of an inversion center in the space groups [49]. Figure 2.5 delineates the ZnO formations of rocksalt, zinc blende, and wurtzite. It was discovered that wurtzite ZnO is made of atoms that form hexagonal-close-pack sub-lattices that stack alternately along the c-axis [50]. In this circumstance, each Zn2+ sublattice includes four Zn2+ ions and is encompassed by for O2- ions , with the edges of a tetrahedron coordinated. This coordination makes polar symmetry along the hexagonal pivot, causing piezoelectricity and unconstrained polarization within the ZnO wurtzite gem [51]. The polarization impact is among of the important elements affecting crystal development amid the ZnO nanostructures. The dim dark and dark circles in Figure 2.5 speak to ZnO and O, separately [52].

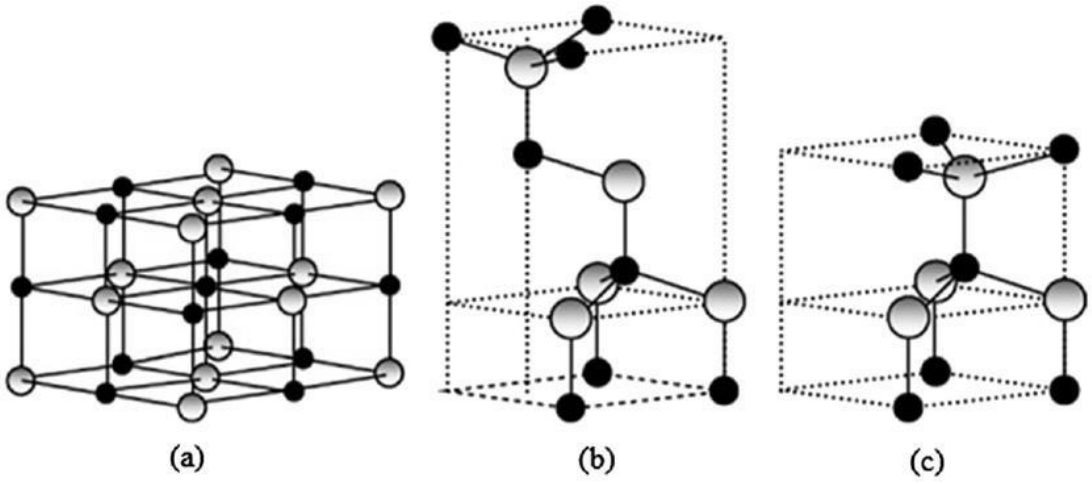

Figure 2.5: The (a) rocksalt (cubic), (b) zinc blende (cubic), (c) wurtzite (hexagonal) structures model of ZnO.

2.2.3 Mechanical properties of ZnO

ZnO ordinarily includes a hardness run of 4 to 5 GPa distinctive spaces [53]. This value must be considered all through the handling and plan of ZnO devices. Indentation of the ZnO lattice significantly reduces excitonic luminescence [54]. As previously stated, the crystal introduction of Zinc oxide resulted in varied mechanical properties. When compared to c-axis oriented ZnO, a-axis bulk ZnO exhibits a reduced hardness of 2 GPa [54, 55]. Studies on epitaxial ZnO has revealed that

epitaxial ZnO developed on sapphire has a better toughness than bulk ZnO [56]. The hardness of c-axis epitaxial layers is 5.75 GPa [57].

2.2.4 Electrical and optical properties of ZnO

At ambient temperature, Zinc oxide incorporates a coordinate band-gap of 3.37 eV and impressive exciton division vitality of 60 meV, as well as great electro-optical characteristics and incredible electrochemical steadiness [58, 59]. ZnO is chemically, thermally, and radiationally stable [58-60]. The, n-type ZnO semiconductor has a large direct band-gap, increased quality of e^- and high breakdown voltages [60, 61]. Because of its superior electrical characteristics, ZnO has been employed primarily in fueled electronic gadgets such as field emanation gadgets. Furthermore, altered ZnO has been utilized as a straightforward conducting cathode in a assortment of optoelectronic gadgets [61]. As a result, ZnO has been utilized in applications like UV/blue light emitter applications [58].

2.2.5 Luminescence and lattice dynamics properties of ZnO

Photoluminescence can be used to characterize ZnO luminescence properties (PL). Typical PL spectra of ZnO nanostructures include two regions: UV emissions and wide visible emissions [62, 63]. UV emission is credited in this scenario to excitons recombination (electron-hole pair recombination or band to band recombination) [40, 64]. UV emission would be extremely great if the ZnO was highly crystalline [64]. The origin of the visible green band in ZnO is linked to numerous impurities and imperfections. The visible emission might be caused by electron recombination with oxygen opening and photoexcited gaps within the valence band, and thus its expanded intensity can be inferable to high imperfection concentration [65]. Raman spectroscopy can be used to measure the lattice dynamics of a single crystal wurtzite ZnO. The 4 atoms per unit cell in a flawless wurtzite ZnO crystal correspond to 12 phonon modes. The modes consist of one longitudinal acoustic (LA), two transverse acoustic (TA), three longitudinal optical (LO), and six transverse optical (TO) branches.

2.2.6 Thermal properties

Thermal growth constant, thermal conduction and specific heat are all thermal characteristics of ZnO. A material's thermal expansion coefficient is the cross section misshapening as a work of temperature. At 300 K, Inc Ocide has warm development co-efficients of a=4.31x10-6 K-1 on the a-axis and a=2.49·10^{-6}·K^{-1}on the c-axis. Thermal conductivity is a material's capacity to transfer heat.This conductivity values within the run of 0.6 W·cm^{-1}·K^{-1} to 1 W·cm^{-1}·K^{-1} is common. The heat capacity per unit mass of material is referred to as specific heat. In fact; the grid vibrations, free carriers, and number of absconds present in a material all influence its specific heat. C_p=40.3 J·mol^{-1}·$K^{-1}$for ZnO at constant pressure [66].

2.2.7 Toxicity of ZnO

ZnO has been utilized as nanoparticles in beauty care products and sun blocker formulations since it is not hazardous to human cells [67]. In comparison to non-nanosized materials, nanoscaled particles improve skin retention, ultraviolet radiation attenuation qualities, and, most importantly, widespread acceptance [68]. It has been proven that when exposed to UV radiation, ZnO can conduct photocatalytic reactions, generating various Reactive Oxygen Species ($O2^{\bullet}$, H_2O_2, and $HO^{\bullet}$) that can induce neural harm and natural poisonous quality [69]. Nanosized ZnO is particularly harmful to many species, including fish [70] and algae [71]. The toxicity is attributed to two effects: oxidative stress caused by the ROS produced and the release of Zn2+ ions [72, 73].

However, nanosized ZnO has been shown to have antibacterial action against a wide range of bacterial species [72]. The hazardous characteristics of ZnO are being investigated in bulk and nanoscale formulations.

According to the literature, antimicrobial characteristics improve when size is reduced up to the nanometer range, as a result of nanosized ZnO will act with each the outside and interior of cells [74]. This feature, on the other hand, must be considered because its discharge into the environment can have an impact on the microbial community in water and soil systems. Microbial colonies help the

environment by biodegrading many types of organic materials [75], as well as act as nitrogen fixers for plants controlling its release into the environment or reducing the toxicity of the nanostructures is a priority in this scenario.

2.3 Porphyrin

Porphyrins are N-heterocyclic molecules found in majority of biosystems that help with e^- and O transport and storage, still as chemical change centers for biotransformation like cytochrome P450. Porphyrin is an aromatic macrocyclic molecule consisted of twenty carbon atoms and four element atoms (Figure2.6). Moreover, the nitrogen molecules of the rings purpose internal to the center, forming a special arrangement capable of binding the bulk of metal ions shaping the several metal complexes, resulting in a category of compounds known as metalloporphyrins once the porphine ring is replaced at the pyrrolic and/or pyrazolic positions [76]. Metalloporphyrins have solely -pyrrolic substituents in biological frameworks and show up connected to proteins, creating supramolecular structures such as hemoglobin, myoglobin, cytochromes, catalases, and peroxidases, similarly as chlorophylls and bacteriochlorophylls once decreased [77, 78].

The nature of the porphyrin ring ensures strong $\pi \rightarrow \pi^*$ electronic transitions in the visible range, significantly in the 400-450 nm range, wherever the Soret band with the very best molar physical property constant seems, taken after by two or four lower concentrated Q-bands within the 500-700 nm range, giving those tetrapyrrolic macrocycles an intense dark purple color.

Porphyrins' intriguing structural, spectroscopic, and photochemical features, and their various activities in biosystems, have piqued the curiosity of experts globally. Anyway, their manufacture, particularly of nonsymmetrical derivatives, was demonstrated to be extremely complex requiring chemists to design techniques for the arrangement of porphyrin subordinates capable of mimicking these features [79-81]. Chlorins, benzoporphyrins, purpurins, texaphyrins, phthalocyanines, naphthalocyanines, and protoporphyrin IX are some examples of porphyrin-type derivatives. In practice, the sphere of porphyrin manufacturing has progressed to the

point wherever nearly any sort of spinoff are often ready, for instance, permiting the conclusion of complex porphyrin structures and materials with fascinating chemical action, chemical science, photophysical, and electrochemical properties. Indeed, those supramolecular materials are often customized with acceptable properties for use in several scientific fields [82-84].

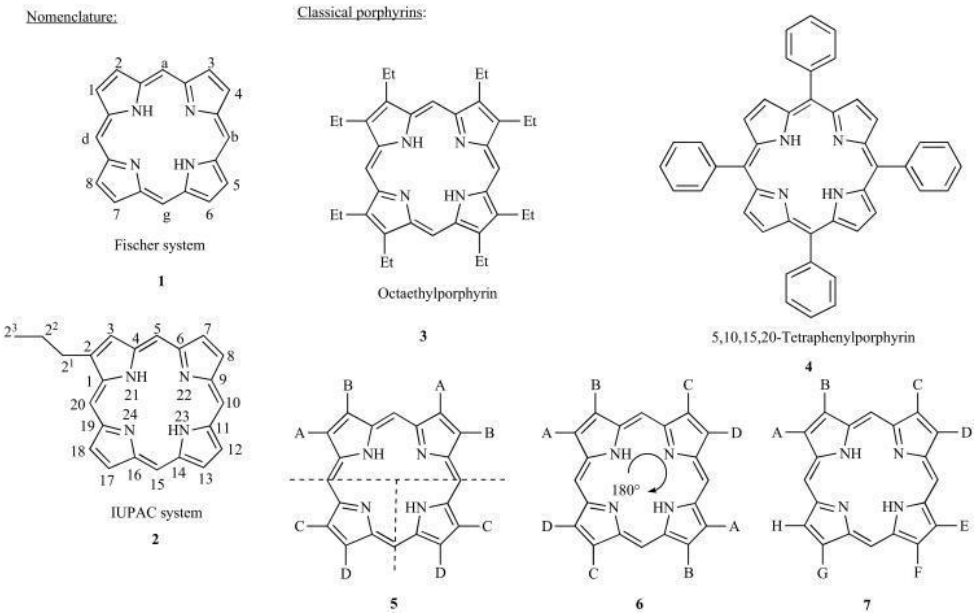

Figure 2.6: Porphyrin nonmeclature [130]

2.3.1 Porphyrin in PDT and imaging

Porphyrin derivatives exhibit negligible toxicity, high tumor uptake, and assimilation within the therapeutic window (600 to 800 nm), furthermore as distinctive photo-physical and photo-thermal properties, creating them promising molecules to be used in medicine, notably photodynamic treatment (PDT) (Figure 2.7). When light is absorbed by the porphyrin, highly reactive species such as singlet oxygen are formed very locally, providing control of the treatment site as a result of it's keen about the presence of both the photosensitizer and lightweight. In fact, singlet oxygen and different reactive species have the ability to destroy bacteria and cancer cells. Another intriguing aspect of porphyrins is their photoinduced fluorescence and phosphorescence, which have been investigated in determination by fluorescence following. Furthermore, porphyrin derivatives metallated with magnet transition metal ions will abbreviate the atomic turn time constant of p^{+} and may well be

utilized for diagnostic purposes using magnetic resonance imaging (MRI) or they will have coordinating sites for diagnostic functions using positron emission tomography/computed tomography (PET/CT) imaging [77, 85-87].

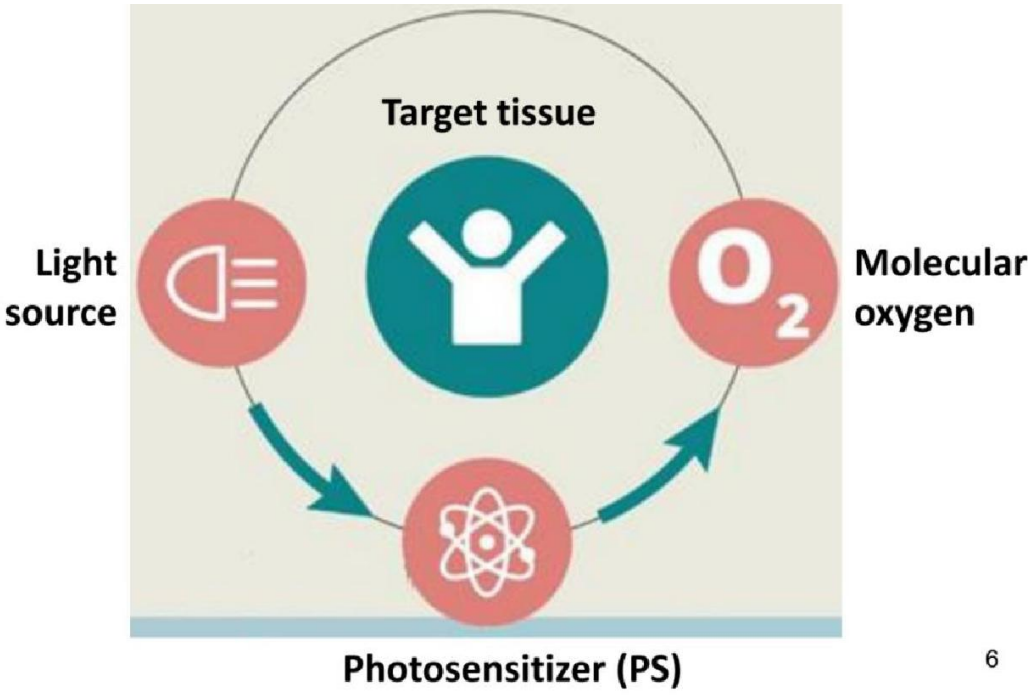

Figure 2.7: Schematic representation of Photodynamic Therapy (PDT)

2.3.2 Porphyrin Dendrimers

Dendrimers have a profoundly branching three-dimensional plan with precisely controllable characteristics, and they show potential as nanocarriers. Dendrimer architecture comprises of three basic design spaces: a multivalent surface, internal shells, and a core. Dendrimers are a versatile nano-scaffold because of the high density of utilitarian bunches on their surface. When the host and guest are hydrophobic and hydrophilic molecules, severally, the inner core will exhibit host-guest interaction that mimics micelle structure. Hydrophobic porphyrin photosensitizers can be applied to the branches or enclosed in the core. Porphyrins can be synthesized in this manner to resemble natural heme-containing proteins. [88, 89]

2.3.3 Porphyrin-Phospholipid Compounds

Porphyrins were first integrated into polymersome nanovesicles in 2005. Later, in 2011, it was shown that by covalently conjugating a porphyrin to the side chain of a phospholipid, the porphyrin-phospholipid may self-assemble into porphysomes, generating a immaculate porphyrin-bilayer. Porphysomes have a good variety of biophotonic applications, like photothermal medical care and PA. Porphyrin-phospholipid micelles show promise as theranostic agents as well. There is an effort in recent years to refine and discover new clinically helpful applications of porphysome technology. The determination and treatment of various forms of cancer has been a major source of innovation [90-92].

2.3.4 Porphyrin Hydrogels

Hydrogels are 3-dimensional networks of deliquescent polymers which will hold a lot of water. Hydrogels are employed in a spread of biological and pharmaceutical applications, together with tissue engineering, drug delivery and PDT [93-96].

Photodynamic antimicrobial chemotherapy (PACT) is a type of PDT that kills germs by using light sensitizing medicines. Because of the flexibleness of hydrogels throughout the assembly method, they will be wrought into varied shapes suitable for various therapeutic circumstances, most commonly around a surgical wound. Following surgery, for example, clinical imaging techniques could be used to monitor the oxygen concentrations round the wound and hypodermic conditions. The porphyrin photosensitizers can also produce singlet oxygen, which can harm microbes, thereby achieving the PACT purpose [97].

2.4 Studies of hybrid materials in cancer cells

2.4.1 Carbon quantum dots and porphyrin

The low solubility, destitute photostability, and accumulation propensity of conventional photosensitizers have hampered their direct application in photodynamic treatment (PDT) of cancer cells. As a result, difficult and time-consuming synthetic techniques, like creating nanomaterials and then loading them

with photosensitizers, have become necessary for the successful utilization of photosensitizers in PDT. In the study of Murali et al., The as-synthesized HP-CQDs retained all of the intrinsic optical and chemical features of HP while exhibiting good water solubility. The capacity of HP-CQDs to generate reactive oxygen species under deep red-light illumination promoted their use in PDT-assisted effective eradication of human breast cancer cells (MCF-7). HP-CQDs had very strong phototoxicity and minimal dark toxicity toward MCF-7 cells when compared to HP. Furthermore, Li et al. discovered a method for hydrothermally synthesizing brilliant luminous N-rich metal-free and metal-doped CQDs employing TPP and its metal complexes as precursors. Their fluid solutions generate vivid blue light when exposed to UV light, and the PL wavelength was red-shifted when excited with longer wavelengths. Furthermore, CQDs and M-CQDs might be used as fluorescent probes to detect Fe3+ ions in aqueous solution in a highly sensitive and selective manner. The MTT experiment on HeLa cells demonstrates CQDs' minimal cytotoxicity. Because of their low toxicity, great biocompatibility, and low detection limits, CQDs can be utilized as efficient probes for cellular particoloured imaging and fluorescent sensors [98].

2.4.2 Zinc Oxide and porphyrin

In the study of Liu et al., a porphyrin subordinate, meso-tetra o-amino phenyl porphyrin MTAP, was attached to ZnO nanoparticles. The vitality exchange rate from Zinc Oxide nanoparticles to MTAP was examined, and it was found to be as high as 83%. In the human ovarian carcinoma cell line NIH: OVCAR-3, ZnO-MTAP conjugates have minimal toxicity however substantial phototoxicity when compared to MTAP and ZnO alone. According to the findings, ZnO-MTAP conjugates could be effective in PDT [99]. Moreover, Photodynamic treatment (PDT) against ovarian cancer has been devised, manufactured, and tested using zinc oxide (ZnO) nanoparticles conjugated to porphyrin (ZnO-MTAP) by Zhang et al. Photoactivation of ZnO-MTAP conjugates, based on the self-lighting photodynamic treatment (SLPDT) concept, will result in the generation of reactive oxygen species, and these ROS can produce selective toxicity. Following production, the nanoparticles were pure by gel exclusion natural process, and their tumoricidal effectuality was tested victimization the human female internal reproductive organ neoplastic cell line NIH: OVCAR-3. Laser scanning confocal

microscopy was intended to monitor cellular uptake of nanoparticle conjugates. ZnO-MTAP conjugates (1-10 M, 24 hr) had low cytotoxic potential within the dark. Ultraviolet light (UVA, 9 kJ/m2) had no influence on cell survival. Co-exposure to UVA radiation (9 kJ/m2) and ZnO nanoparticle conjugates, on the opposite hand, resulted in dose-dependent cytotoxicity (40% and 92%, respectively). Furthermore, caspase 3/7 activity was significantly increased 3-6 hours after irradiation, indicating that phototherapy promoted apoptosis. These findings demonstrate that photoactivation of ZnO-MTAP is really promising for cancer treatment [100].

2.5 Characterization Methods

2.5.1 Raman Spectroscopy

Raman spectroscopy is a useful tool for investigating sample quality in wide band gap semiconductors, as well as specialized aspects such as isotopic effects. The Raman spectra of produced products are sensitive to crystal quality, structural flaws, and diseases. Light scattering experiments examine its spectral distribution in relation to the spectrum of incidental light. The peaks of the spectrum in scattering Raman and Brillouin situations are energy extremely close to the energy of incident light, but several orders of magnitude smaller in intensity. As a result, it is required to limit the light scattered tires. Light sources are lasers, and the analysis is done with double and triple monochromators. When compared to a simple monochromator, the discrete capacity and rejection of light dispersed tires is much improved. The Rayleigh criterion is used to define the discrete barrier monochromatic capacity, which is as follows (Eq 2.1):

$$R0 = \frac{\lambda}{\Delta\lambda} = \frac{\lambda Fm}{Wdcos\theta} \quad (2.1)$$

Where:

- F: the length of the spectrometer,
- W: the slit width,
- 1/d: the barrier constant,

• m: the order fringe of contribution,

• θ: the angle of incidence at the dam

If the peaks of the spectrum are only a few wavelengths apart from the stimulating laser beam, the analysis requires the use of Fabry-Perot interferometers, as is common in Brillouin spectroscopy [112]. The Laser beam is focused on the sample with an appropriate lens to achieve good resolution and high intensity. Figure 2.8 depicts several Raman geometries: a) scattering geometry 90^{o} for transparent crystals (incident intensities and scattered light are doubled using mirrors M1 and M2), b) scattering geometry 90^{o} for highly absorbent materials, c) improved geometry: the laser beam is guided using a small mirror between a focusing lens and the material under study, d) rear geometry 180^{o} (the direction of propagation incident and scattered light is precisely determined, facilitating the application of selection rules), e) In the case of photosensitive laser beams, use a cylindrical focusing lens of the laser beam (this reduces the power density of the laser beam on the sample without reducing the efficiency of the scattered light focused with the cylindrical lens the entire length of the spectrometer input slot).

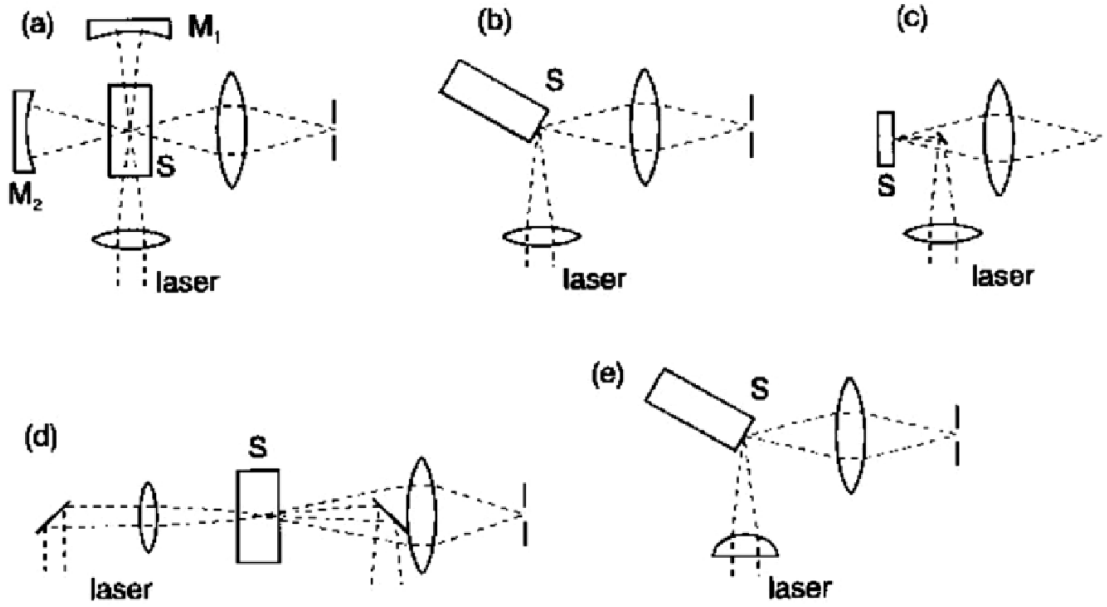

Figure 2.8: Raman geometries

Raman scattering occurs when the polarity of molecules or the electrical sensitivity of crystals changes. Under the influence of an external electric field E(, the

polarization o of the atomic orbitals results in the formation of a bipolar moment PD(ω)= αoE(ω).If the molecule oscillates with frequency, the distance between atoms A and B varies on a regular basis, and the polarity is molded by (Eq.2.2-2.3)

$$PD(\omega) \rightarrow = (ao + a1\ cos\Omega t)\ Eo \rightarrow cos\ cos\ \omega \quad (2.2)$$

$$PD \rightarrow = ao\ \ Eo \rightarrow cos\ cos\ \omega t + (\alpha 1\ E0\ 2\ )\ [cos(\omega + \Omega)t + cos(\omega - \Omega) \quad (2.3)$$

In addition to the frequency, the re-emitted light carries the frequencies + and - .Because the visible is on the order of 20000 cm-1, and phonon frequencies can be very low, on the order of several cm-1, displacements ± Ω with respect to can be very small. Furthermore, the 2nd order polarity, 1, is substantially less than the 1st order polarity order, o, indicating that the side bands are weak.

In crystals, the scattering process is more complicated, since re-emitted waves face a periodic structure and contribute enhancers for (Eq. 2.4):

$$2\Lambda sin\frac{\theta}{2} = n\lambda \quad (2.4)$$

where:

• Λ and λ are the phonon and photon wavelengths respectively,

• n the indicator refraction,

And

• θ the angle between the scattering and the incident beam

The energy of the non-scattered light tires is smaller or bigger than the energy of the input photon depending on whether the phonon is stimulated or absorbed, thus scattering processes are classified as scattering Stokes (ω-Ω) and Anti Stokes (ω+Ω). The Raman spectrum of silicon (Si) is shown in Figure 2.9, with typical peaks Stokes and Anti Stokes symmetrically organized in terms of exceptionally strong top of the tyre scattered light. Rayleigh scattering is another name for elastic scattering.

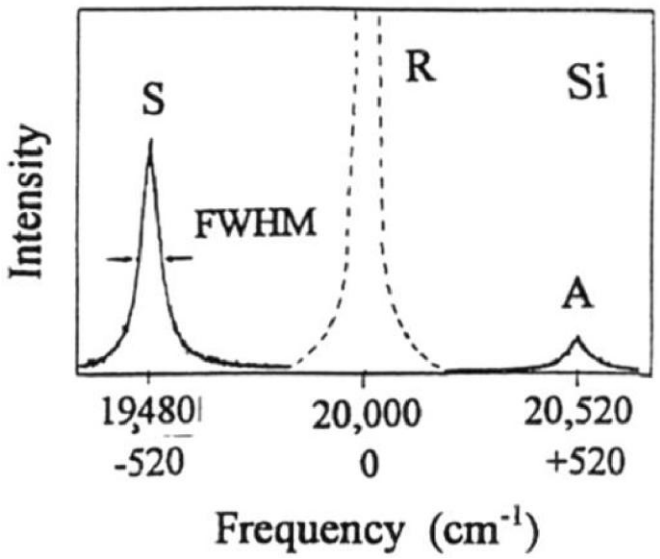

Figure 2.9: Si Raman spectra [112]

A phonon can only contribute to Raman scattering if it induces a change in polarity, which is determined by mechanical deformation caused by the external field in the molecule or unit crystal cell [112].

It is recognized for symmetrical diatomic, asymmetric diatomic and symmetric triatomic molecules whose deformations result in a change in polarity. Furthermore, the geometric deformations cause a shift in the molecule's bipolar torque PD. Infrared oscillations of this sort are active (excited) (IR). The polarization changes during the oscillation of diatomic molecules and its symmetrical style of oscillation of three-atom molecules, hence these oscillations are known as Raman active. In contrast, for asymmetric oscillations of triatomic molecules, the derivative of polarity with respect to normal variable Q is zero for Q=0, indicating that the corresponding oscillations are Raman inactive. The same is true for infrared oscillations. The oscillations of asymmetric diatomic molecules and asymmetric triatomic molecules cause a shift in bipolar moment and are hence IR-active. Asymmetric molecular oscillations are obviously Raman and IR active [112].

2.5.2 Dynamic Light Scattering (DLS)

The technique determines the "hydrodynamic" particle size, which is the prevalent size among irregularly shaped particles dispersed in liquid media and corresponds to

the real average size in cases with known particle form, such as spherical [101]. The method is based on changes in the intensity of visible light scattered by nanoparticles dispersed in a liquid media and performing Brownian random motion. During the measurement, a laser directs a monochromatic radiation beam to a tiny volume of liquid, and the intensity of the scattered light is recorded by a sensor situated at a given angle to the incident radiation, the wavelength of light, and the dispersant's diffraction index (Figure 2.10). The scattering vector can be calculated using the equation (Eq.2.5).

$$q = \frac{4\pi n}{\lambda} sin\ sin\ \frac{\theta}{2} \quad (2.5)$$

where:

• λ is the wavelength and

• θ is the angle

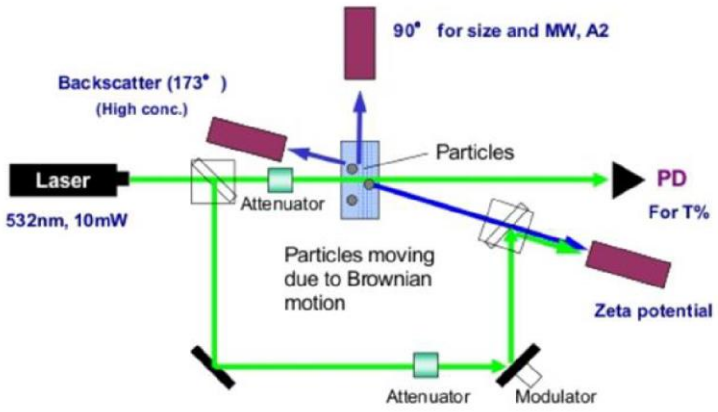

Figure 2.10: Schematic illustration of DLS.

A diluted representative sample is usually tested to limit the amount of reflected rays. The Stokes-Einstein relation (Eq. 3.6) gives the diffusion constant for particles with average radius R:

$$D = \frac{kT}{6\pi\eta R} \quad (2.6)$$

where:

- k is the Boltzmann constant,
- T is the mean temperature and
- n is the viscosity.

Variations in the strength of the reflected radiation are noticed as the particles move randomly, as the measured intensity varies with particle position. As a result, the measurement time period is also critical, such that the particle positions do not change dramatically [102]. According to Eq. 3.7, the connection with particle size drops exponentially over time:

$$g^1(t) = exp\ (-q^2 D_1) \quad (2.7)$$

where $g^1(t)$ denotes the first order normalized correlation between the diffraction vector q and the constant refraction D. A linear combination of refraction for each component is obtained by making repeated measurements at different angles (Eq.2.8):

$$g^1(t) = \sum_{i=1}^{n} \quad exp(-q^2 D_i) A_i \quad (2.8)$$

where

- D is the diffusion index by weight or quantity of each component

In the case of multi-scattering systems, the relation is thus simplified to its final form.

$$g^1(t) = exp(-q^2 D_t)(1 + K1 + K2 + \cdots)$$

where:

- K1, K2 are the sums of the components.

Dynamic light scattering devices provide direct information on component size for a wide variety of dimensions ranging from about 1nm to around 10 m. The amplitude of the particle size dispersion is then determined by the polydispersity index (PDI). It specifically spans from 0 to 1, with 0 representing single-dispersion systems and 1 representing dispersion [102]. A technique known as light scattering phase analysis is used to characterize the potential. When a laser beam is passed through a sample to

record the velocity of the particles when a given electrical voltage is put on the solution, the findings are analyzed using the Smoluchowski methodology for polar solvents. As the absolute value of the surface potential grows, the measured load on the particle surfaces provides increasing electrostatic forces that keep the system in dispersion, resulting in increased system stability over time.

2.5.3 X-Ray Diffraction (XRD)

X-rays are electromagnetic radiation with wavelengths ranging from 0.1 to 100. Wavelengths ranging from 0.7 Mo to 1.54 Cu are extensively employed in crystal structure. They are formed when fast-moving charged particles are usually electron-retarded, but they can also be produced by radioactive isotopes like 55Fe. The latter are almost entirely employed for performance regulation rather than data collection via diffraction. Generators with sealed closed tubes (lamps), open spinning anode tubes, or synchrotron radiation rings are used. Both the closed and open ones operate in vacuum, with the open ones being able to be disassembled for repair. In the optical area, the study of the spectrum and the distribution of energy at different wavelengths is mostly accomplished by two methods:

- refraction from prisms and/or
- diffraction from a suitable barrier.

Because both procedures are difficult, the primary method of spectrum study relies on X-ray diffraction by crystals that behave as natural three-dimensional barriers. This application of crystals is a direct result of Bragg's interpretation of the diffraction effect as the reflection of the incident beam from the crystal's multiple lattice levels. One of the most significant advances in science is X-ray diffraction. Because the wavelengths of the X-rays are approximately equivalent to the distances between the atoms in the crystal, diffraction is examined more in crystallography. When X-rays are enclosed in a crystal, they function as crystal structure constructors, according to William L. Bragg. Reflection is the scattering of light from a two-dimensional continuous material, such as a plane of atoms in a crystal structure.

However, the terms diffraction and reflection are interchangeable. If X-rays strike an atom plane at an angle of incidence, the rays will penetrate the layers of atoms and produce their picture. Absorption, fluorescence, and diffraction are three features of X-rays that have practical use in material investigation [114]. The powder method approach is the most widely used industrial and laboratory (research) use of X-ray diffraction. To be examined, the sample does not need to be in powder form. Only the granules that make it up must be a few microns (m) in size. Plate samples are analyzed with ease and satisfactory results. Qualitative analysis, quantitative analysis X-ray (XRD), structure analysis, tension determination in metals, particle size determination, identification and evaluation of raw materials are all possible applications for diffraction. When a monocrystal is irradiated, it must be circled in three distinct dimensions so that all levels progressively come into a corner reflection (Bragg relation) and give all conceivable reflections. If only one surface of the crystal is irradiated, and that surface can rotate along an axis parallel to it, i.e., there is a potential of angle change (Bragg angle), then essentially only one plane will come at an angle and test the Bragg relation, giving the associated reflection. In practice, zone reflections, i.e., first-order reflections and multiples of them, appear (Figure 2.12).

The XRD method is based on the diffraction of monochromatic X-ray radiation of known wavelength (λ) on the crystal levels of the analyzed materials, followed by the determination of the internal intervals d of the crystal lattice levels that are unique to each chemical (Figure 2.11) [115]

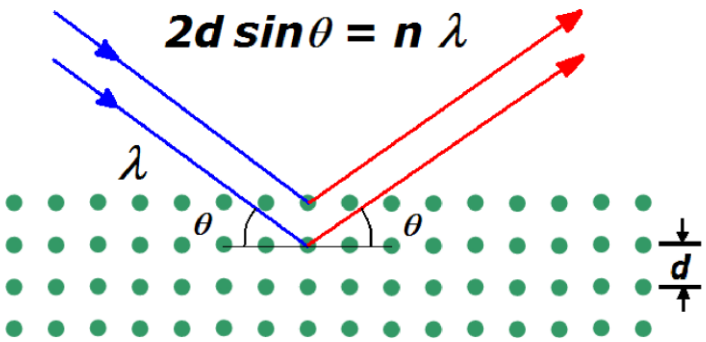

Figure 2.11: Bragg law

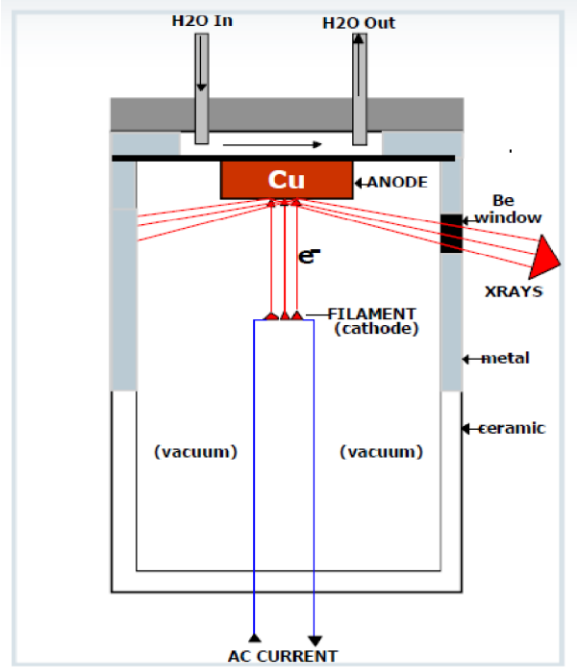

Figure 2.12 : Basic functioning of an XRD instrument [115]

An XRD diagram initially determines whether the material is crystalline or amorphous. Long, sharp peaks can be seen in crystalline diagrams. Furthermore, the XRD method provides information on a compound's crystal structure and is employed in mineralogical research. It also offers information on crystal imperfections in ultrapure (crystalline compounds). It measured the degree of crystallinity (the percentage of crystalline material in a given material) in substances such as pharmaceuticals, food, and polymers. Furthermore, it is used to identify polymorphism and quantify distinct phases [115].

2.5.4 UV-Visible Spectroscopy

Ultraviolet-visible (UV-Vis) spectroscopy refers to qualitative and quantitative analyses that reveal important information for chromophore (=light absorbing groups) of molecules via electronic transitions of molecular orbitals in the range 190-780nm. Absorption spectroscopy characterizes a wide range of materials by using the energy gap caused by radiation of a specific wavelength. In particular, at a given photon energy, electrons are excited and a transition from the valence layer to a higher conductivity layer occurs [113]. The intensity of absorbed or reflected radiation in relation to the wavelength of excitation characterizes the different

components of the material and aids in understanding its structure [113]. The breadth of the peaks is determined by the size of the nanoparticles as well as their size dispersion.

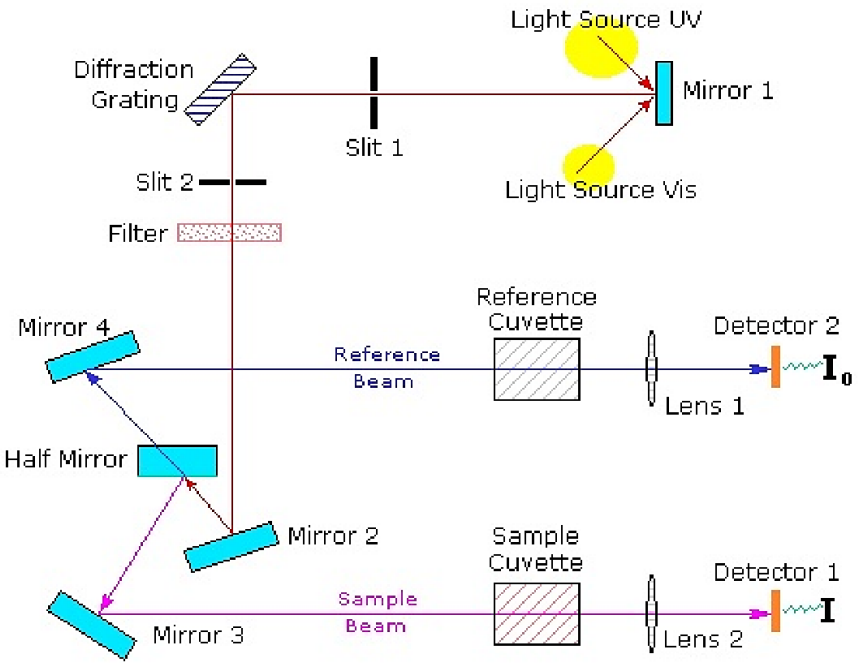

Figure 2.13: Typical functioning of a UV-Visible spectrometer

Figure 2.13 depicts a diagram of a typical spectrometer. The operation of spectrometer is pretty simple [116]. A crystal or diffraction grinding isolates a light-bar from a UV light source into its component wavelengths. A device isolates each monochromatic (single wavelength) pillar into two break even with escsalated pillars. The intensity of the light beams are measured. I0 is that the intensity of the reference beam, that ought to have had tokenish or no light-weight absorption. *I* denotes the intensity of the sample beam. The ultraviolet (UV) area is typically scanned from 200 to 400 nm, while the visible section is typically scanned from 400 to 800 nm [117].

Transmittance (T = I/I0) and absorbance (A= logI0/I) are two ways to specific retention. In the event that no assimilation has happened, T=1.0 and A=0. Most spectrometers display absorbance on the vertical axis.The wavelength of maximum absorbance is a characteristic value denoted as λ max.

2.5.5 Fourier- Transformed Infrared (FTIR)

The introduction of Fourier transformation infrared spectrophotometers, which superseded ordinary scatter spectrophotometers, was responsible for the true revolution in infrared spectroscopy [117]. Because of their high sensitivity and speed, the usage of these instruments has gradually increased in recent decades to a considerably wider number of applications. A standard FTIR spectrophotometer with a Michelson interferometer is made up of three major components: an infrared source, an interferometer, and an infrared detector. The laser source is utilized to provide an internal reference, measure wavelengths, and fine-tune the pulse duration [117].

The medium infrared sources utilized by FTIR spectrophotometers are the same as those employed by conventional IR spectrophotometers (Globar or Nerst lamps). When considering the far infrared region (FIR), a high-pressure mercury lamp can be utilized, whereas tungsten-halogen lamps are typically employed for the near infrared (NIR) range. The interferometer is the heart of the FTIR spectrophotometer, and its utilization offers substantial advantages over capturing the IR spectrum with a monochromator. The Michelson interferometer, depicted in Figure 2.14, is one of the most frequent and widely used interferometers. It consists of two mirrors M1 and M2, one of which remains stationary (mirror), while the other either moves at a constant mirror speed or stops regularly and for brief periods of time (moving mirror). The levels of the two mirrors are perpendicular to each other, and there is a 50/50 beam splitter between the fixed and moving mirrors. The beam separator is a translucent mirror made of material that does not absorb infrared light and has a reflectivity and permeability of 50%. The beam splitter material is chosen based on the spectrum range under consideration. Beam separators used in the NIR and FIR regions are often made of potassium bromide or cesium iodide substrates coated with materials such as germanium or iron oxide, whilst thin organic films (such as polyethylene) are utilized in the far infrared spectrum [117].

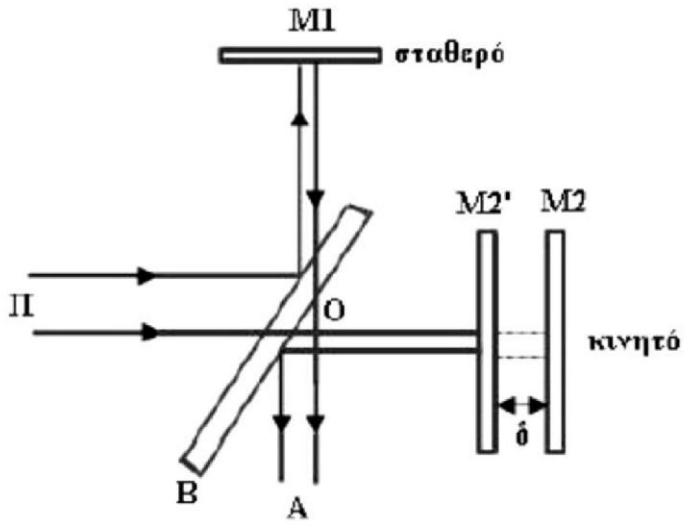

Figure 2.14: Schematic illustration of a Michelson symbolometer, where Π: the source, M1: mixing mirror, M1': reflection of M1 as seen from position A, M2: movable mirror, B: beam divider (chopper) and A: analyzer.

Infrared radiation released by the source is directed to the separator, where it separates into two bundles, the one falls on the constant mirror and the other on the mobile phone, and then returns to the bundle separator, where it contributes. After a parcel of the radiation is coordinated to the test chamber, the remainder is directed back to the source radiation [118]. As a result, even though they took different trajectories, roughly half of each bundle ends up in the detector. The contrast (δ) between the optical paths of the two light bars is 2 (OM2 - O2'). When the source emits a continuous frequency range, the signal strength as the delay function I'(δ) is provided by the following relation:

$$I'(\delta) = 2\int_0^\infty I(v)(1 + cos2\pi v\delta)dv = 2\int_0^\infty I(v)cos2\pi v\delta dv$$

which it appears that the intensity I '(δ) consists of a constant factor and one variable 2 I(v)cos2dv 0 who is accountable for the interferogram's look. The notation is a space-time domain spectrum (time domain spectrum) that captures changes in the detector's response (intensity) as a function of time during the mirror scan and gives information for the whole infrared spectral area in which the detector responds. The notation is mathematically processed using the Fourier transform before being

translated to the received IR spectrum, which displays the intensity as a function of frequency (frequency domain spectrum).

DTGS (deuterated triglycine sulfate) detectors made of deuterated triglycine sulfate and MCT detectors built of tellurium cadmium telluride mercury cadmium tellurium are the two most prevalent types of detectors used in FTIR spectroscopy. Most detectors employing standard IR spectrophotometers (such as thermocouples) have too sluggish a response time for the quick scan times of interferometers [128]. The DTGS detector is a pyroelectric detector that operates at room temperature and has a fast response time since it measures temperature changes rather than temperature values. The MCT detector, which belongs to the group of photon detectors and is based on the quantum nature of radiation, operates at 77 K and has a faster reaction and greater sensitivity than the DTGS detector.

The great sensitivity and speed of FTIR spectrophotometers, as well as the enhanced signal-to-noise ratio (SNR) per unit time (Fellget advantage) [103], provide them a distinct edge over traditional IR spectroscopy techniques. This advantage is due to their core design and operation characteristics, which allow a full spectrum to be collected during a single mirror scan, while the detector can see all frequencies at the same time. Because of its fast scanning speed, many spectra may be captured in a very short period of time (1 minute or less), and sensitivity can be considered. Furthermore, these instruments often employ a circular optical aperture that permits a broad beam area to pass through the sample, resulting in signal amplification and enhanced SNR (Jacquinot advantage) ratio. In addition, when combined with the infrared light incident on the Michelson interferometer, the HeNe laser beam provides the capacity to precisely record the displacement of the moving mirror while also determining the number of repeating spectra. Finally, the use of a computer in FTIR spectroscopy allows for the rapid capture of many spectra and the processing of data using a wide range of accessible processing algorithms, resulting in the recording of very high-quality spectra [117]. The superiority of FT-IR spectrophotometers is due to their basic construction and operation characteristics, which result in:

- All frequencies emitted by the source reaching the detector at the same time,
- A large area of the beam passing through the sample, and
- The precise position of the moving mirror [117].

3. Materials and Methods

3.1 Materials

Deionized water was distilled in the lab, using a MILLI-Q® HX 7000 SD device (Greece - Merck S.A. Hellas, an affiliate of Merck KGaA, Darmstadt, Germany, Athens, Greece). Sodium hydroxide (NaOH) and citric acid (CA) were purchased from Lachner (Techline SA, Athens, Greece) and graphite rods from Meusburger (Meusburger, Wolfurt, Austria). Zinc acetate dehydrate (CH_3COO_2) $Zn.2H_2O$ was used as the source of Zn. Zinc acetate dehydrate was purchased from Penta (Penta, Kappa Lab, Athens, Greece). Calcium chloride solution from Sigma Aldrich (Greece - Merck S.A. Hellas, an affiliate of Merck KGaA, Darmstadt, Germany, Athens, Greece). 4-Carboxybenzaldeyde, 96% and Pyrrole, 99% extra pure and Ethanol (EtOH) absolute 99.8%, which was used to the solution, were purchased from Fischer Scientific U.K. Limited, Acros Organics Jansen Pharmaceutical and Dialysis Membrane-150, LA401 from Himedia (HiMedia Laboratories GmbH, Einhausen, Germany). MDA-MB-231 (human epithelial breast adenocarcinoma, highly invasive - ATCC - LGC Standards GmbH, Wesel, Germany - HTB26™), MCF-7 (Michigan Cancer Foundation (MCF)-7 (epithelial breast adenocarcinoma, low metastatic potential - ATCC - LGC Standards GmbH, Wesel, Germany - HTB-22™), A549 (human epithelial lung carcinoma - ATCC - LGC Standards GmbH, Wesel, Germany - CCL-185™) and HEK293 (normal human epithelial kidney embryonic cells - ATCC - LGC Standards GmbH, Wesel, Germany - ACRL-1573™) cell lines were cultured in Dulbecco's modified Eagle's medium (DMEM) (Gibco BRL, Life Technologies, Thermo Scientific, Paisley, United Kingdom), supplemented with 10% fetal bovine serum (FBS) (Gibco BRL, Life Technologies, Thermo Scientific, Paisley, United Kingdom), 1% L-glutamine, 1% sodium pyruvate, and antibiotics (Gibco BRL, Life Technologies, Thermo Scientific, Paisley, United

Kingdom) for the experimental needs, incubated at 37 °C in a 5% CO_2 incubator. In addition, trypsin–Ethylenediaminetetraacetic acid (EDTA): 0.05%/0.02% (w/v) (Gibco BRL, Life Technologies, Thermo Scientific, Paisley, United Kingdom) were used for the trypsinization of cells.

3.2 Methods

3.2.1 Electrochemical process of carbon quantum dots

Sonication was used to remove large particles from the surface of graphite rods that had a diameter equal to 3.5 nm and a length equal roughly to 60 nm. Next, the graphite rods were immersed in the electrolyte and used as anode and cathode electrodes. The electrolyte used was a water-based combination of citric acid monohydrate (0.1 M) and NaOH (0.3 M) (100 mL). Cyclic voltammetry (CV) was performed before chronoamperometry and utilized to wet the graphite electrodes in a voltage range from -1 to +5 V. Then, the chronoamperometry was performed for 30 minutes at a voltage of +10 V and a current of 0.14 Ampere. As a consequence, the electrolyte solution changed color from colorless to yellow, verifying the graphite rod. Once this reaction was completed, 0.15 M calcium chloride was added to the generated solution. This solution was heated up to 68°C to precipitate calcium citrate. The calcium citrate precipitate was separated by centrifugation twice at 9.000 rpm for 10 minutes. After, membrane filtration (pore size of around 2.4 nm) was used to filter the supernatant for 7 days in order to remove the salt from the solution [104].

3.2.2 Preparation of the ZnO NPs

A sample was prepared by using the zinc acetate dehydrate $(CH_3COO_2)Zn.2\ H_2O$ (Mr=219.5 g/mol) as precursor. To begin making a 0.15 M zinc acetate solution, 3.2925 g of zinc acetate dehydrate were weighed and added to 100mL of distilled water, which was then agitated with a magnetic stirrer until it became homogeneous. The initial pH value was approximately 6.65. Then, drop by drop, 0.1

M was added until the solution acquired a milky-white look. The final pH level was nearly 13. The milky-white solution was then left in 50°C for 2 hours. The recovered white sediment was centrifuged three times for ten minutes at 9000 rpm. To eliminate organic residues, the white sediments were rinsed in between the centrifuges twice with water and once with ethanol absolute 99.8%. The recovery was dried for 1 hour at 100°C before being annealed for 3 hours at 400°C. A mortar is used to grind the finished product. For convenience, the finished product shall be referred to as ZnAc. A mortar is used to grind the finished product. For convenience, the finished product shall be referred to as ZnAc [105].

3.2.3 Synthesis of TCPP

The synthesis of TCPP (meso-tetra (4-carboxyphenyl)porphyrin) is done via Adler method according to the literature [106].

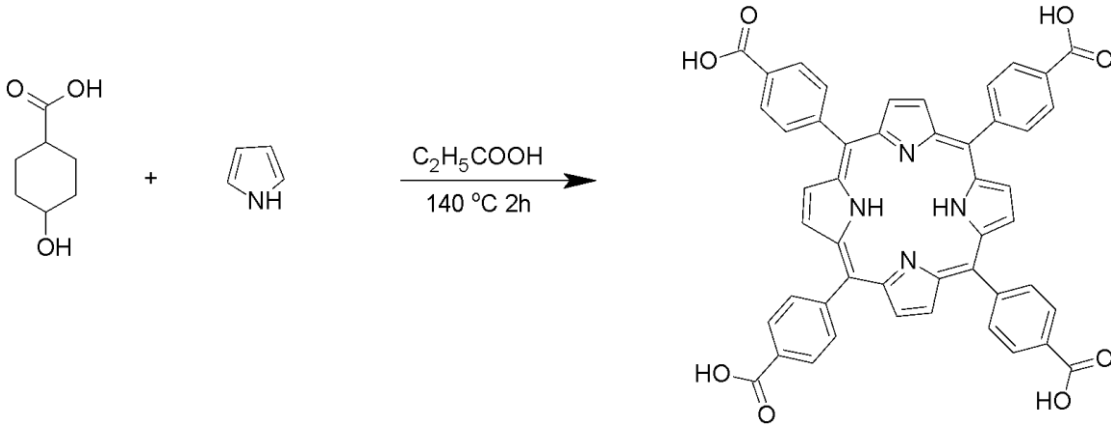

In a round bottom flask, 300.3 mg o f4-carboxybenzaldedyde (2 mmol) in 10 ml of propionic acid were dissolved. Then 140 µl pyrrole(2 mmol) was added. The reaction was left under stirring 140°C for 2 hours and its progress was monitored by TLC. After the reaction was over, the flask was transferred to the freezer to help precipitate the solid. This was followed by vacuum filtration with DCM and water. A dark solid was obtained.

3.2.4 Synthesis of ZnO-porphyrin 2.5 %

In a round bottom flask, 50 mg of porphyrin were weighed and added to 200 ml of methanol, which was then agitated with a magnetic stirrer until the porphyrin is dissolved. Then 2 g of Zno were added to the mixture and the vessel was sealed with

parafilm to prevent the methanol from evaporating. The mixture was left stirring for a day. Then, it was centrifuged for 3 more times. The precipitate was left and the plate was placed in the oven at 60°C to dry. The finished product is ground in a mortar [107].

3.2.5 Cell culture

The cell lines human embryonic kidney 293 (HEK293), the breast cancer cell lines MCF7 and MDA-MB-231 and the lung cancer cell lines A549 were cultured in Dulbecco's Modified Eagle Medium (DMEM) High Glucose culture media, which contained 10% Fetal bovine serum (FBS), 100U/ml penicillin, 100g/ml streptomycin, and 2 mmol/L glutamine.

The culture was carried out at 37°C. The culture media was replaced every two days, and cells were passaged once a week with normal trypsin EDTA doses. The cells were then frozen in a freezing medium containing FBS and 10% dimethyl sulfoxide (DMSO) [108].

3.2.6 MTT Colorimetric Assay

MTT assay is a colorimetric assay used to assess cell metabolic movement. The MTT assay's biological mechanism involves a NAD(P)H-dependent cellular oxidoreductase enzyme that transforms the yellow tetrazolium MTT [3-(4,5-dimethylthiazolyl-2)-2,5-diphenyltetrazolium bromide] (Thiazolyl Blue Tetrazolium Bromide M5655, Sigma-Aldrich, Darmstadt, Germany) into the insoluble (E,Z)-5-(4,5-dimethylthiazol-2-yl)-1,3-diphenylformazan (formazan). The generated formazan can be dissolved in dimethyl sulfoxide (DMSO) or DMSO solutions to produce a purple hue with 570 nm absorbance. ~8.000-10.000 cells were used for each tested sample. The rate of cell reasonability was assessed as a % ratio of treated cells to untreated cells.

The concentration of the purple color is specifically relative to the number of cells, demonstrating cell viability. The active mitochondrial hydrogenases of living cells cleave and convert the soluble yellow dye to the insoluble purple.

Various types of control samples were used, namely a positive control (cells treated with cis-platin 0,75 mg/ml), negative control (cell untreated), extra negative control (cell irradiated only without NPs) and blind sample (nutrient medium alone). The experiment was repeated four times in triplicate with similar results.

4. Results

4.1 Characterization of CQDs

1. Dynamic Light Scattering (DLS)

The Dynamic Light Scattering (DLS) instrument (Zeta Sizer nano S, Malvern Inst., Malvern, UK) is used to measure the size and distribution of particle size, potential g, and molecular weight using a laser wavelength of 633 nm and a scattering angle of 173^{o}. The instrument operates at temperatures ranging from 0 to 90°C, with special sections inside that regulate the temperature for measurements of potential g and particle size in a particle dispersion solution.

The average size of the CQDs was discovered to be 45 nm (Figure 4.1), which is slightly larger than expected from the literature. The CQDs zeta potential has a single peak at negative 39.4 mV (Figure 4.2). The negative potential denotes the presence of negative charge moieties on the surface of C-QDs. Such moieties are required for a good dispersion of C-QDs in a water-based solvent [109].

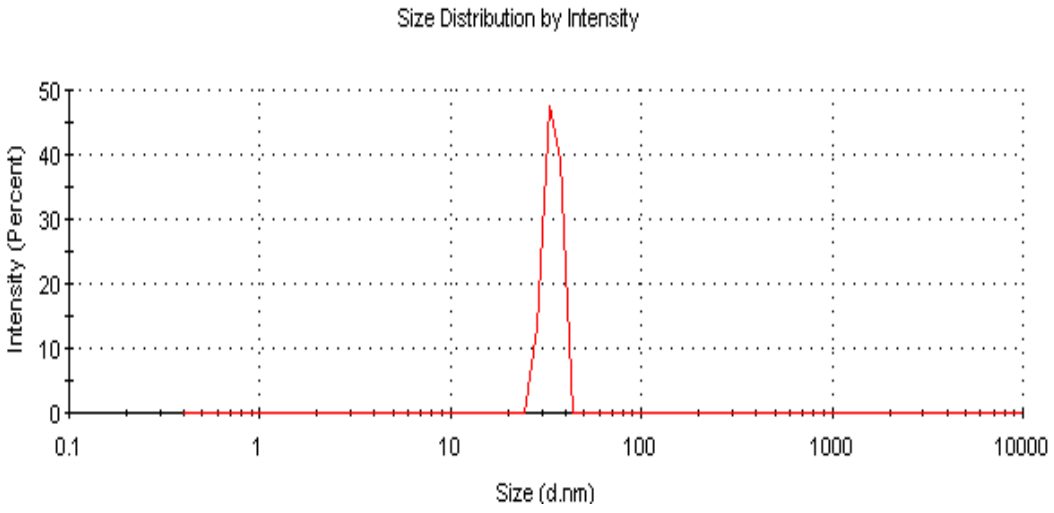

Figure 4.1: Size distribution diagram for CQDs

		Mean (mV)	Area (%)	St Dev (mV)
Zeta Potential (mV): -39.4	Peak 1:	-39.4	100.0	5.53
Zeta Deviation (mV): 5.53	Peak 2:	0.00	0.0	0.00
Conductivity (mS/cm): 0.0115	Peak 3:	0.00	0.0	0.00

Result quality : Good

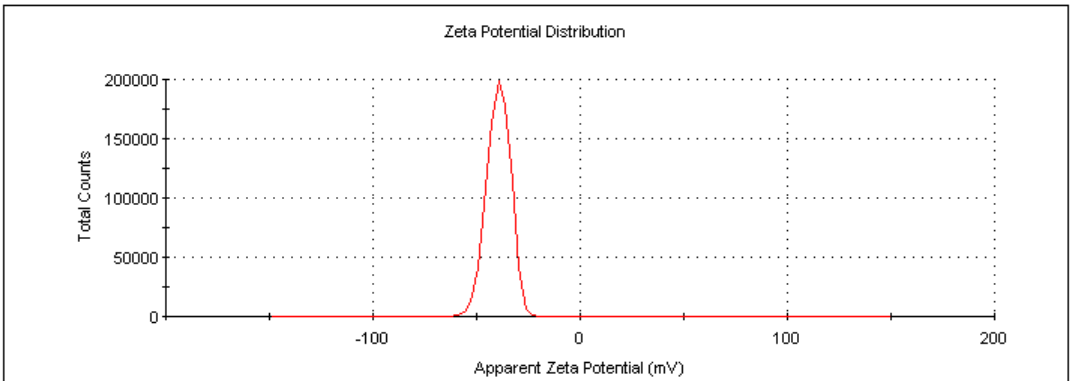

Figure 4.2: Zeta potential distribution for CQDs

2. UV-Visible Spectroscopy

The UV-Visible spectroscopy was conducted using the Hitachi U-2001 Spectrophotometer.

The CQDs exhibited typical UV/Vis absorption at 230 nm which could be ascribed to the π→π* transition of the aromatic sp2 domain within the CQDs [137], and another minor shoulder peak at 283 nm attributed to the n-π* transition of C=O bond [110] (Figure 4.3).

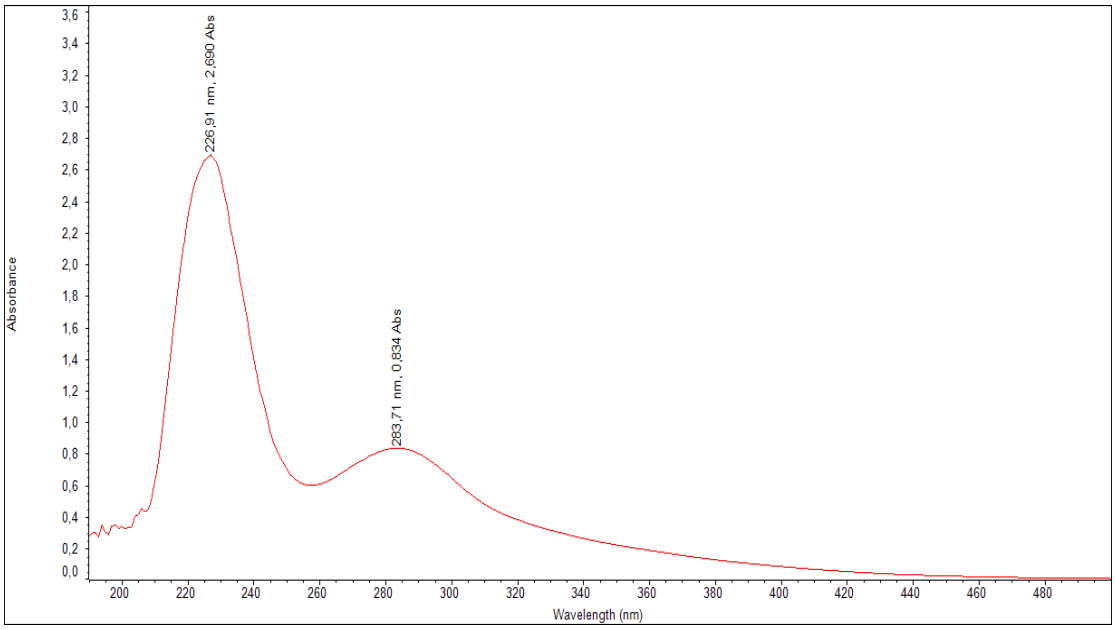

Figure 4.3: UV-Vis diagram for CQDs

3. FTIR

The FTIR instrument used is the FTIR JASCO4200, using Ge crystal.

FTIR spectra of CQDs have significant peaks at 3243,1727,1589,1434 and 995 cm^{-1} (Figure 4.4) .

These peaks can be ascribed to OH, C=O, C=C, and C-H bending [139],[140].The presence of a C=C peak indicates that the C-QDs have a graphitic structure, whereas the presence of OH, C=O, and C-H bending peaks indicates that the C-QDs have OH, C=O, and C-H surface moieties attached to their surface.

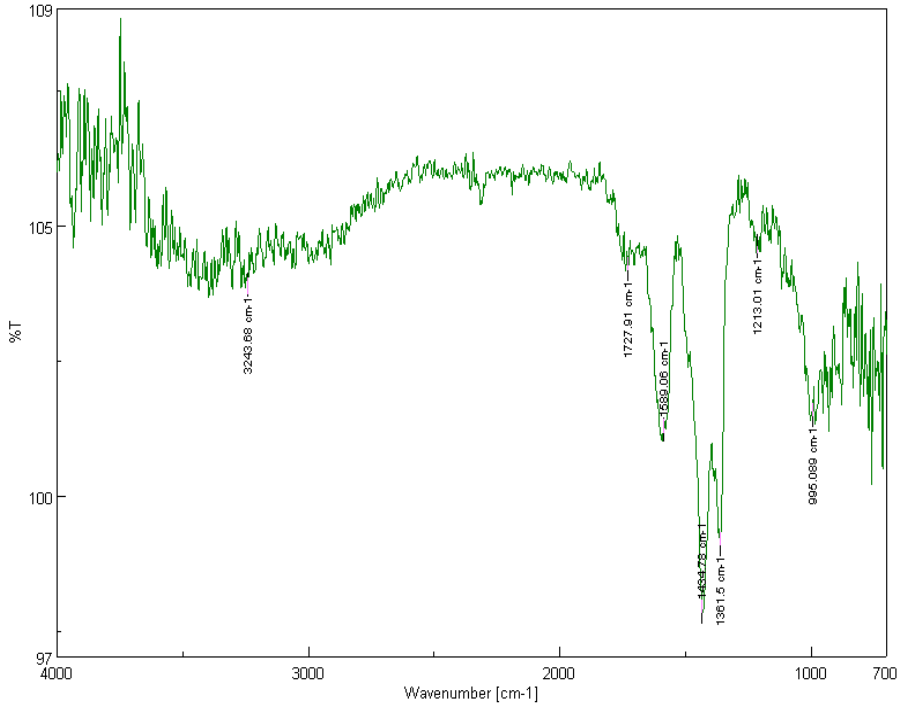

Figure 4.4: FTIR diagram for CQDs

4.2 Characterization of ZnO-TCPP NPs

1. UV-Visible Spectroscopy

UV- Vis ZnO has a single peak at 380 nm, while ZnO-TCPP have one smaller peak at 430 nm. This indicates probably the conjugation of the ZnO with the porphyrin (Figure 4.5).

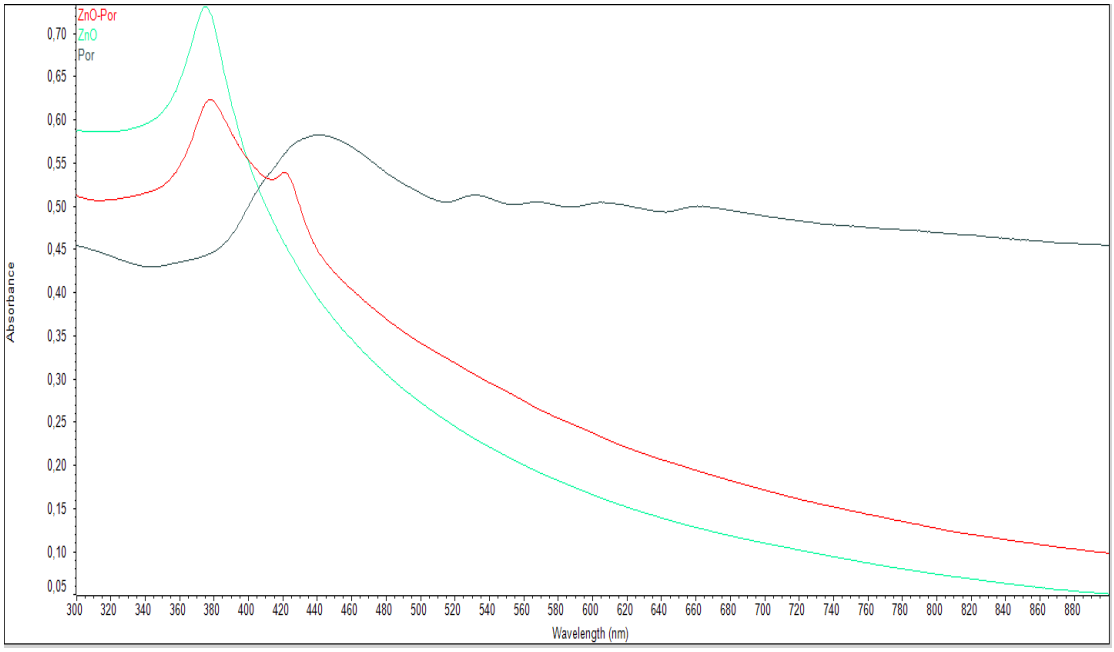

Figure 4.5: UV-Vis diagram for ZnO, porphyrin, ZnO-porphyrin

2. X-RAY DIFFRACTION (XRD)

Crystallinity was defined using X-Ray diffraction (XRD) (Figure 4.6) The X-Ray Diffractometer is a Brücker D8 Advance. The measurements were conducted at a 2-theta angle with a range of 20° to 80° and a scanning rate 0.01°/0.5 sec, employing Cu-Kα radiation (λ = 1.5418 Å) at a voltage of 30 kV and a current of 15 mA.

When the ZnO was measured all of the indexed peaks in the obtained spectrum match those of bulk ZnO (JCPDS Card No. 36-1451), confirming that the synthesized powder is single crystalline and has a wurtzite hexagonal structure. Within the detection limit of the X-ray diffraction, no other impurity-related peak was detected in the spectrum, confirming that the synthesized powders are pure ZnO. Peaks formed at 31.81°, 34.34°, 36.29°, 47.57°, 56.63°, 62.89°, 66.43°, 67.95°, 69.07°, and 72.6° correspond to the planes (100), (002), (101), (102), (110), (103), (200), (112), (201), and (004), respectively. Peak intensity and partly small width indicate a high degree of crystalline production.

But when the ZnO-TCPP was measured, a peak at 11 that does not yield ZnO and a very small one between 30-35 appeared implying that it is not pure ZnO, but has impurities.

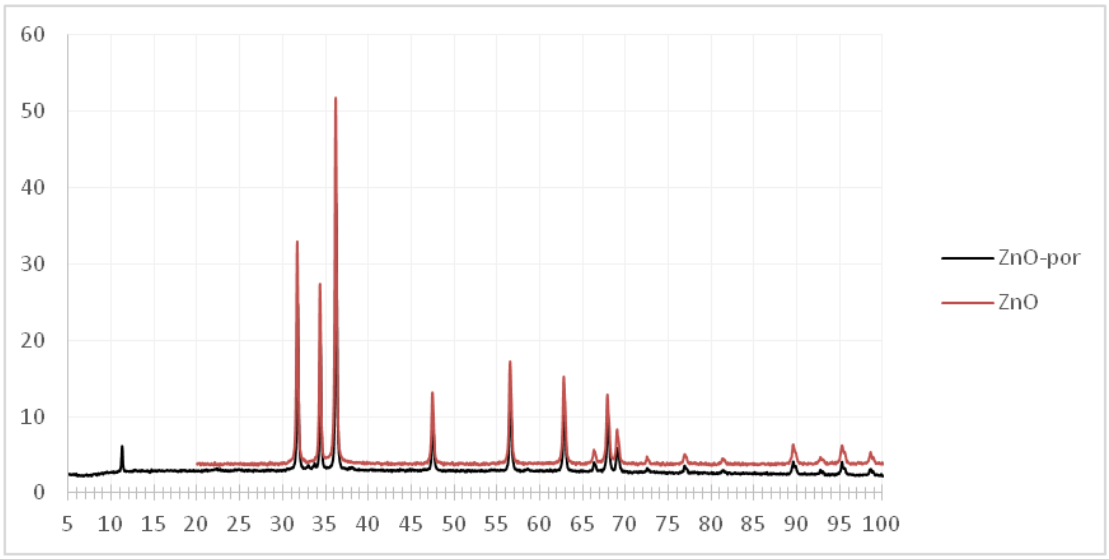

Figure 4.6: XRD diagram for ZnO, Zno-porphyrin

4.3 Toxicity studies

4.3.1 Toxicity studies of CQDs

Incubation of the HEK293, A549, MDA-MB-231 and MCF-7 with CQDs and an MTT measurement after 24 hours post treatment in a concentration of 25mg/ml resulted in 100% viability in HEK293, MDA-MB-231, MCF-7 and 97% viability in A549, while 99% viability was observed after incubation with 75mg/ml. The results are shown in the following table (Figure 4.7). These findings indicate that CQDs are not toxic.

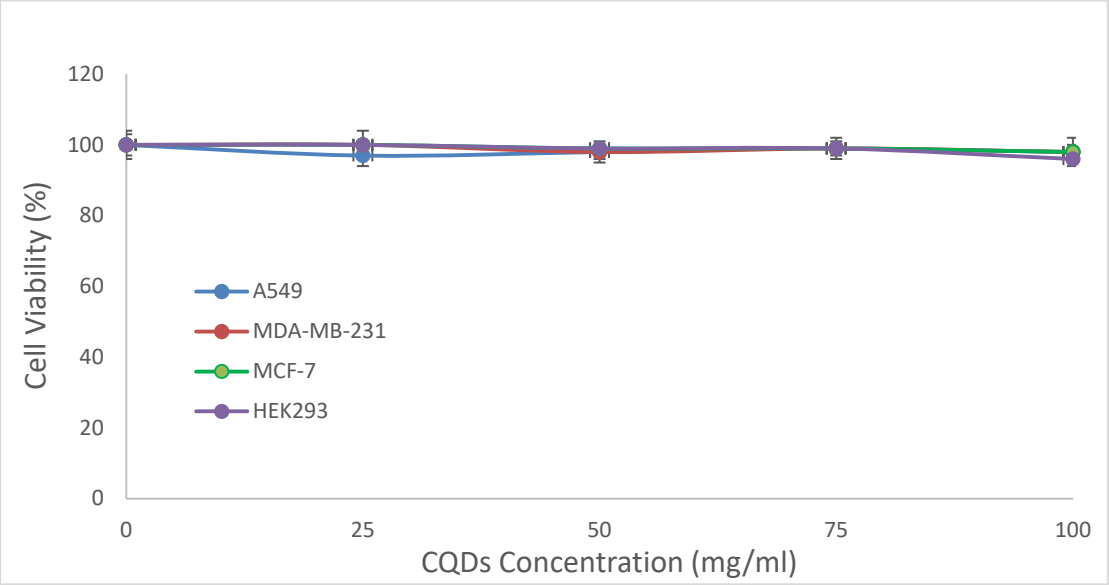

Figure 4.7: CQDs viability assay in HEK293, MDA-MB-231, MCF7, A549

4.3.2 Toxicity studies of porphyrin

Incubation of the HEK293, A549, MDA-MB-231 and MCF-7 with porphyrin in a concentration of 25 mg/ml resulted in 100% viability, while 99% viability was observed in A549, MDA-MB-231 and 97% viability in MCF7, HEK293 after incubation with 100mg/ml. The MTT assay was performed after 24 hours post treatment. These results who are shown in the following table (Figure 4.8) declare the no toxicity of porphyrin.

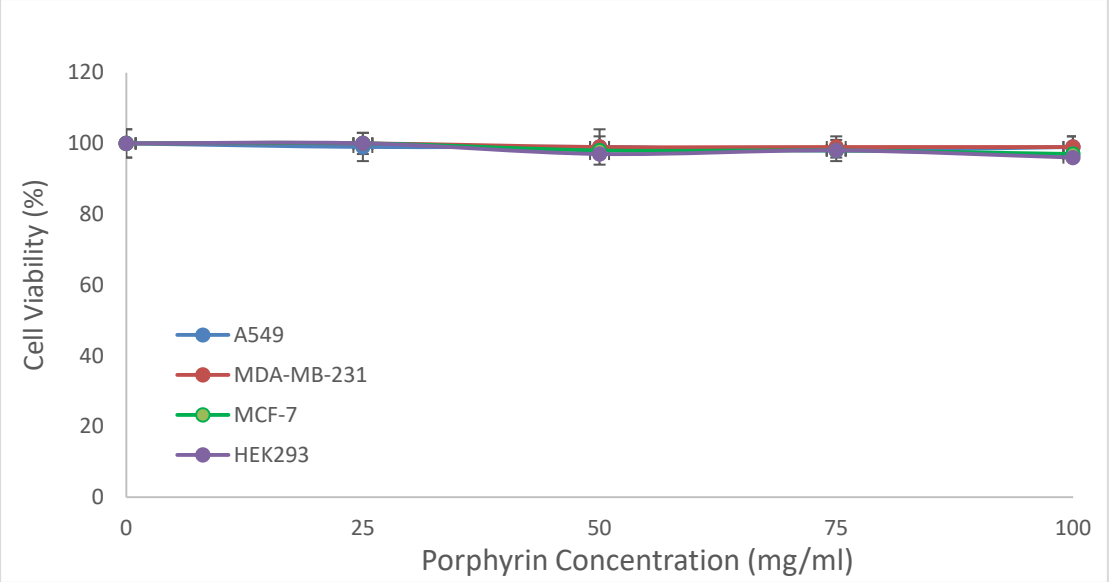

Figure 4.8: Porphyrin viability assay in HEK293, MDA-MB-231, MCF7, A549

4.3.3 Toxicity studies of ZnO

Incubation of the HEK293, A549, MDA-MB-231 and MCF-7 with ZnO in a concentration of 25mg/ml resulted in 90% viability in A549, 95% in MDA-MB-231 and 100% in MCF-7 and HEK293. In a concentration of 75mg/ml, viability was measured at 79% in A549, 88% in MDA-MB-231, 97% in MCF7 and 98% in HEK293. These MTT measurements which were performed after 24 hours post treatment (Figure 4.9) show that ZnO has no effect on normal cells, but have the ability to kill cancer cells A549 and MDA-MB-231. As long as for the combination of ZnO-porphyrin, porphyrin didn't change the activity of ZnO.

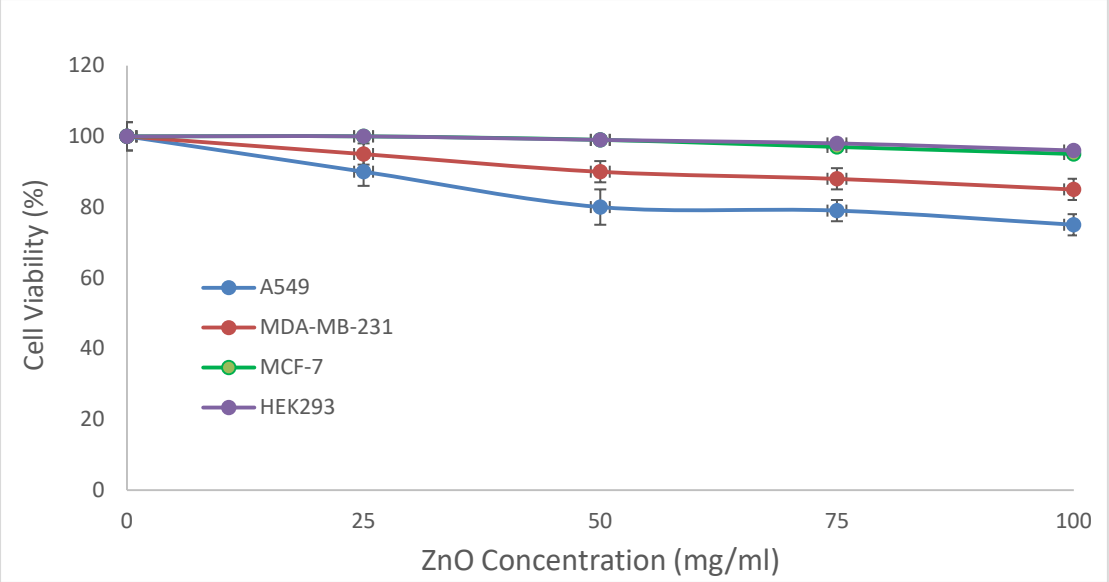

Figure 4.9: ZnO viability assay in HEK293, MDA-MB-231, MCF7, A549

4.3.4 Toxicity studies of ZnO-UV

Upon irradiation with UV-A light (350 nm) for 10 minutes and incubation of the HEK293, A549, MDA-MB-231 and MCF-7 with ZnO in a concentration of 25mg/ml in A549, MDA-MB-231, MCF7, HEK293 resulted in 75%, 85%, 95% and 98% respectively, while in a concentration of 100mg/ml the results were impressing, since the viability was 50% in A549, 60% in MDA-MB-231, 85% in MCF7 and 93% in HEK293. These MTT measurements whish were performed after 24 hours post treatment and their results which are shown in the next table (Figure 4.10) indicate that UV photoactivation improved the activity of ZnO in cancer cells, while in normal cells HEK293 was much less toxic.

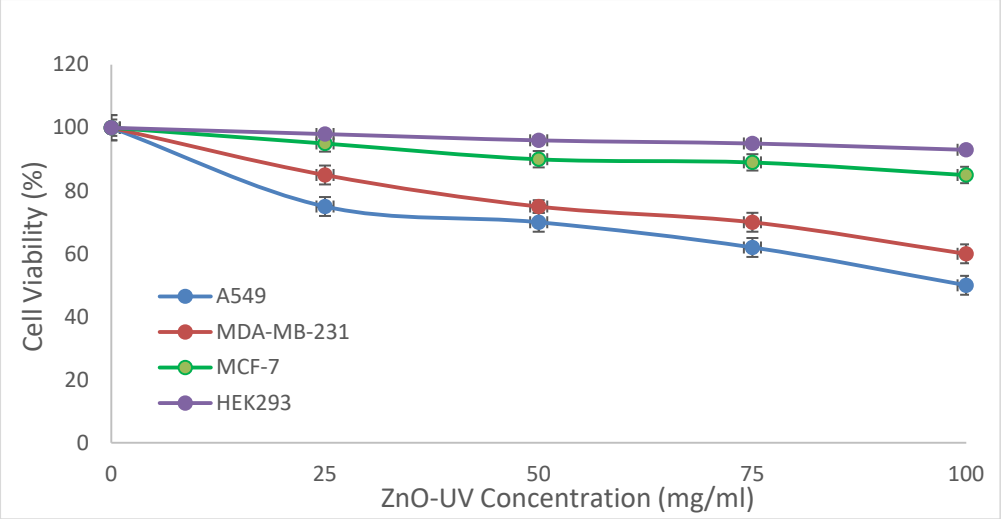
120
100
80
60
40
20
0
Cell Viability (%)
A549
MDA-MB-231
MCF-7
HEK293
0
25
50
75
100
ZnO-UV Concentration (mg/ml)

5. Discussion-Conclusions

Cancer is a multifaceted disease and a cause of death worldwide [1]. Scientists approach cancer in some ways, but there are still aspects of the analysis field of other cancer treatments that stay to be discovered, specializing in diminution of the undesirable consequences of the standard treatment strategies [2]. In this study, a hybrid material consisted of CQDS, ZnO and porphyrin was proposed, which would ideally become a theranostic material.

The motivation of this experimental study is to build knowledge and generate expertise in a multidisciplinary field, lying on materials science, chemical engineering, and biomedicine.

CQDs have the potential to become the following generation of green nanomaterials. Due to their tiny size, sensible biocompatibility and optical performance, their good water dispersibility in water and excellent fluorescence properties, therefore it's a new material for molecular imaging [14]. Electrochemical process, which was performed in this study, is a low cost, simple operation, high yield and good reproducibility method. The production of carbon quantum dots directly generated from electrochemical oxidation of graphite electrodes in alkaline alcohols is quite innovative. Also, their toxicity results in normal cell lines HEK293 and cancer cell lines A549, MCF-7 and MDA-MB-231 showed that they are not toxic, making them even more promising for imaging material.

Porphyrin, which was processed via Adler method, is a really common photosensitizing agent that is especially localized in mitochondria, resulting in programmed necrobiosis upon lightweight exposure [111]. Porphyrin's derivatives have outstanding photophysical and photothermal properties making them promising molecules to be employed in medicine, especially photodynamic therapy (PDT) [91]. Moreover, the cytyotoxicity results of porphyrin in cell lines HEK293, A549, MCF-7 and MDA-MB-231 indicated the no toxicity of porphyrin.

ZnO nanoparticles, with their unique properties like biocompatibility, increased toxicity and high selectivity is a promising anticancer agent. Research has shown that

low zinc concentration in cells leads to the initiation and progression of cancer and high zinc concentration shows toxic effects. The selective localization of ZnO nanoparticles to cancer cells because of enhanced permeability and retention effect (EPR) make them a potential antitumor agent [7, 8]. The toxicity results of ZnO in cancer cells showed that ZnO can kill cancer cells A549 and MDA-MB-231(especially after UV rradiation), but not normal cells HEK231, results which are very encouraging.

To conclude, this hybrid material could become a material for imaging and therapy, but since it is a quite innovative proposal, it still needs experimental effort until it can be optimized and used.

6. References

1. Meng, X., et al., *A new hypothesis for the cancer mechanism.* Cancer Metastasis Rev, 2012. **31**(1-2): p. 247-68.
2. Pucci, C., C. Martinelli, and G. Ciofani, *Innovative approaches for cancer treatment: current perspectives and new challenges.* Ecancermedicalscience, 2019. **13**: p. 961.
3. Effron, J.S., H. Aliazzi, and J. Garcia-Zuazaga, *Current Evidence and Applications of Photodynamic Therapy in Dermatology.* Journal of the Dermatology Nurses' Association, 2015. **7**(3): p. 145-151.
4. Borgia, F., et al., *Early and Late Onset Side Effects of Photodynamic Therapy.* Biomedicines, 2018. **6**(1).
5. Allison, R.R. and K. Moghissi, *Photodynamic Therapy (PDT): PDT Mechanisms.* Clin Endosc, 2013. **46**(1): p. 24-9.
6. Vitti, E.T. and J.L. Parsons, *The Radiobiological Effects of Proton Beam Therapy: Impact on DNA Damage and Repair.* Cancers (Basel), 2019. **11**(7).
7. Kruger, C.A. and H. Abrahamse, *Utilisation of Targeted Nanoparticle Photosensitiser Drug Delivery Systems for the Enhancement of Photodynamic Therapy.* Molecules, 2018. **23**(10).
8. Bisht, G. and S. Rayamajhi, *ZnO Nanoparticles: A Promising Anticancer Agent.* Nanobiomedicine (Rij), 2016. **3**: p. 9.
9. Liu, M., et al., *Carbon quantum dots directly generated from electrochemical oxidation of graphite electrodes in alkaline alcohols and the applications for specific ferric ion detection and cell imaging.* Analyst, 2016. **141**(9): p. 2657-64.
10. Desmond, L.J., A.N. Phan, and P. Gentile, *Critical overview on the green synthesis of carbon quantum dots and their application for cancer therapy.* Environmental Science: Nano, 2021. **8**(4): p. 848-862.
11. Molaei, M.J., *A review on nanostructured carbon quantum dots and their applications in biotechnology, sensors, and chemiluminescence.* Talanta, 2019. **196**: p. 456-478.
12. Devi, P., S. Saini, and K.H. Kim, *The advanced role of carbon quantum dots in nanomedical applications.* Biosens Bioelectron, 2019. **141**: p. 111158.
13. Lim, S.Y., W. Shen, and Z. Gao, *Carbon quantum dots and their applications.* Chem Soc Rev, 2015. **44**(1): p. 362-81.
14. Liu, M.L., et al., *Carbon dots: synthesis, formation mechanism, fluorescence origin and sensing applications.* Green Chemistry, 2019. **21**(3): p. 449-471.
15. Wang, Y. and A. Hu, *Carbon quantum dots: synthesis, properties and applications.* Journal of Materials Chemistry C, 2014. **2**(34).
16. Reyes, D., et al., *Laser Ablated Carbon Nanodots for Light Emission.* Nanoscale Res Lett, 2016. **11**(1): p. 424.

17. John, V.L., Y. Nair, and T.P. Vinod, *Doping and Surface Modification of Carbon Quantum Dots for Enhanced Functionalities and Related Applications.* Particle & Particle Systems Characterization, 2021. **38**(11).
18. Arul, V. and M.G. Sethuraman, *Hydrothermally Green Synthesized Nitrogen-Doped Carbon Dots from Phyllanthus emblica and Their Catalytic Ability in the Detoxification of Textile Effluents.* ACS Omega, 2019. **4**(2): p. 3449-3457.
19. Carolan, D., et al., *Environmentally friendly nitrogen-doped carbon quantum dots for next generation solar cells.* Sustainable Energy & Fuels, 2017. **1**(7): p. 1611-1619.
20. Geng, D., et al., *Nitrogen doping effects on the structure of graphene.* Applied Surface Science, 2011. **257**(21): p. 9193-9198.
21. Zhu, L., et al., *State-of-the-Art on the Preparation, Modification, and Application of Biomass-Derived Carbon Quantum Dots.* Industrial & Engineering Chemistry Research, 2020. **59**(51): p. 22017-22039.
22. Li, Z., et al., *Fluorine-containing graphene quantum dots with a high singlet oxygen generation applied for photodynamic therapy.* J Mater Chem B, 2020. **8**(13): p. 2598-2606.
23. Luo, P.G., et al., *Carbon-based quantum dots for fluorescence imaging of cells and tissues.* RSC Advances, 2014. **4**(21).
24. Eda, G., et al., *Blue photoluminescence from chemically derived graphene oxide.* Adv Mater, 2010. **22**(4): p. 505-9.
25. Demchenko, A.P. and M.O. Dekaliuk, *Novel fluorescent carbonic nanomaterials for sensing and imaging.* Methods and Applications in Fluorescence, 2013. **1**(4).
26. Shen, J., et al., *Facile preparation and upconversion luminescence of graphene quantum dots.* Chem Commun (Camb), 2011. **47**(9): p. 2580-2.
27. Shen, J., et al., *One-pot hydrothermal synthesis of graphenequantum dots surface-passivated by polyethylene glycol and their photoelectric conversion under near-infrared light.* New J. Chem., 2012. **36**(1): p. 97-101.
28. Mathioudakis, C., et al., *Electronic and optical properties of a-C from tight-binding molecular dynamics simulations.* Thin Solid Films, 2005. **482**(1-2): p. 151-155.
29. Chang, Y.P., et al., *Tracking bio-molecules in live cells using quantum dots.* J Biophotonics, 2008. **1**(4): p. 287-98.
30. M.J. Saxton, K. Jacobson (1997), Single-particle tracking: applications to membrane dynamics, Annu. Rev. Biophys. Biomol. Struct. 26 373–399.
31. Bhunia, S.K., et al., *Carbon nanoparticle-based fluorescent bioimaging probes.* Sci Rep, 2013. **3**: p. 1473.
32. Zhang, M., et al., *Magnetofluorescent Fe3O4/carbon quantum dots coated single-walled carbon nanotubes as dual-modal targeted imaging and chemo/photodynamic/photothermal triple-modal therapeutic agents.* Chemical Engineering Journal, 2018. **338**: p. 526-538.
33. S.-T. Yang, L. Cao, P.G. Luo, F. Lu, X. Wang, H. Wang, M.J. Meziani, Y. Liu, G. Qi, Y.-P. Sun,(2009) Carbon dots for optical imaging in vivo, J. Am. Chem. Soc. 131 (32) 11308–11309.

34. Tao, H., et al., *In vivo NIR fluorescence imaging, biodistribution, and toxicology of photoluminescent carbon dots produced from carbon nanotubes and graphite.* Small, 2012. **8**(2): p. 281-90.
35. Hua, X.W., Y.W. Bao, and F.G. Wu, *Fluorescent Carbon Quantum Dots with Intrinsic Nucleolus-Targeting Capability for Nucleolus Imaging and Enhanced Cytosolic and Nuclear Drug Delivery.* ACS Appl Mater Interfaces, 2018. **10**(13): p. 10664-10677.
36. Ge, J., et al., *Red-Emissive Carbon Dots for Fluorescent, Photoacoustic, and Thermal Theranostics in Living Mice.* Adv Mater, 2015. **27**(28): p. 4169-77.
37. Nie, L. and X. Chen, *Structural and functional photoacoustic molecular tomography aided by emerging contrast agents.* Chem Soc Rev, 2014. **43**(20): p. 7132-70.
38. Janotti, A. and C.G. Van de Walle, *Fundamentals of zinc oxide as a semiconductor.* Reports on Progress in Physics, 2009. **72**(12).
39. Peng, W.Q., et al., *Synthesis and temperature-dependent near-band-edge emission of chain-like Mg-doped ZnO nanoparticles.* Applied Physics Letters, 2006. **88**(10).
40. Sharma, B.K., N. Khare, and D. Haranath, *Photoluminescence lifetime of Al-doped ZnO films in visible region.* Solid State Communications, 2010. **150**(47-48): p. 2341-2345.
41. Schmidt-Mende, L. and J.L. MacManus-Driscoll, *ZnO – nanostructures, defects, and devices.* Materials Today, 2007. **10**(5): p. 40-48.
42. Anandan, S., N. Ohashi, and M. Miyauchi, *ZnO-based visible-light photocatalyst: Band-gap engineering and multi-electron reduction by co-catalyst.* Applied Catalysis B: Environmental, 2010. **100**(3-4): p. 502-509.
43. Hasnat, M.A., et al., *Adsorption and photocatalytic decolorization of a synthetic dye erythrosine on anatase TiO2 and ZnO surfaces.* J Hazard Mater, 2007. **147**(1-2): p. 471-7.
44. Peternel, I.T., et al., *Comparative study of UV/TiO2, UV/ZnO and photo-Fenton processes for the organic reactive dye degradation in aqueous solution.* J Hazard Mater, 2007. **148**(1-2): p. 477-84.
45. Behnajady, M.A., N. Modirshahla, and R. Hamzavi, *Kinetic study on photocatalytic degradation of C.I. Acid Yellow 23 by ZnO photocatalyst.* J Hazard Mater, 2006. **133**(1-3): p. 226-32.
46. Gomez-Solís, C., et al., *Rapid synthesis of ZnO nano-corncobs from Nital solution and its application in the photodegradation of methyl orange.* Journal of Photochemistry and Photobiology A: Chemistry, 2015. **298**: p. 49-54.
47. Baruah, S. and J. Dutta, *Hydrothermal growth of ZnO nanostructures.* Sci Technol Adv Mater, 2009. **10**(1): p. 013001.
48. Moore, D. and Z.L. Wang, *Growth of anisotropic one-dimensional ZnS nanostructures.* Journal of Materials Chemistry, 2006. **16**(40).
49. Maggard, P.A., Stern, S.L., Poeppelmeier, K.R., 2001. Understanding the role of helical chains in the formation of noncentrosymmetric solids. J.Am. Chem. Soc. 123 (31), 7742- 7743.
50. Erhart, P. and K. Albe, *Diffusion of zinc vacancies and interstitials in zinc oxide.* Applied Physics Letters, 2006. **88**(20).

51. Kong, X.Y., Wang, Z.L., (2003) Spontaneous polarization-induced nanohelixes, nanosprings and nanorings of piezoelectric nanobelts. Nanno Lett. 3 (12), 1625-1631.
52. Wang, Z.L., *Zinc oxide nanostructures: growth, properties and applications.* Journal of Physics: Condensed Matter, 2004. **16**(25): p. R829-R858.
53. Fang, T.-H., W.-J. Chang, and C.-M. Lin, *Nanoindentation characterization of ZnO thin films.* Materials Science and Engineering: A, 2007. **452-453**: p. 715-720.
54. Zhang, X., et al., *Effect of aspect ratio and surface defects on the photocatalytic activity of ZnO nanorods.* Sci Rep, 2014. **4**: p. 4596.
55. Jian, S.-R., et al., *Surface Morphological and Nanomechanical Properties of PLD-Derived ZnO Thin Films.* Nanoscale Research Letters, 2008. **3**(5).
56. Hwang, D.-K., et al., *ZnO thin films and light-emitting diodes.* Journal of Physics D: Applied Physics, 2007. **40**(22): p. R387-R412.
57. Coleman, V.A., et al., *Mechanical properties of ZnO epitaxial layers grown on a- and c-axis sapphire.* Applied Physics Letters, 2005. **86**(20).
58. Lu, J.G., et al., *ZnO quantum dots synthesized by a vapor phase transport process.* Applied Physics Letters, 2006. **88**(6).
59. Tan, S.T., et al., *Blueshift of optical band gap in ZnO thin films grown by metal-organic chemical-vapor deposition.* Journal of Applied Physics, 2005. **98**(1).
60. Liu, K., M. Sakurai, and M. Aono, *ZnO-based ultraviolet photodetectors.* Sensors (Basel), 2010. **10**(9): p. 8604-34.
61. Umar, A., *Growth of Comb-like ZnO Nanostructures for Dye-sensitized Solar Cells Applications.* Nanoscale Res Lett, 2009. **4**(9): p. 1004-1008.
62. Wang, H.Q., et al., *Polychromatic visible photoluminescence in porous ZnO nanotubes.* Journal of Physics D: Applied Physics, 2007. **40**(21): p. 6549-6553.
63. Hong, W.-K., et al., *Electrical Properties of Surface-Tailored ZnO Nanowire Field-Effect Transistors.* IEEE Transactions on Electron Devices, 2008. **55**(11): p. 3020-3029.
64. Hullavarad, S., et al., *Persistent Photoconductivity Studies in Nanostructured ZnO UV Sensors.* Nanoscale Res Lett, 2009. **4**(12): p. 1421-7.
65. Kurbanov, S., W.C. Yang, and T.W. Kang, *Kelvin Probe Force Microscopy of Defects in ZnO Nanocrystals Associated with Emission at 3.31 eV.* Applied Physics Express, 2011. **4**(2).
66. Sun, X.W., et al., *Heat capacity of ZnO with cubic structure at high temperatures.* Solid State Communications, 2006. **140**(5): p. 219-224.
67. Juliano, C. and G. Magrini, *Cosmetic Ingredients as Emerging Pollutants of Environmental and Health Concern. A Mini-Review.* Cosmetics, 2017. **4**(2).
68. Serpone, N., D. Dondi, and A. Albini, *Inorganic and organic UV filters: Their role and efficacy in sunscreens and suncare products.* Inorganica Chimica Acta, 2007. **360**(3): p. 794-802.
69. Lewicka, Z.A., et al., *Photochemical behavior of nanoscale TiO2 and ZnO sunscreen ingredients.* Journal of Photochemistry and Photobiology A: Chemistry, 2013. **263**: p. 24-33.
70. Chen, T.H., C.C. Lin, and P.J. Meng, *Zinc oxide nanoparticles alter hatching and larval locomotor activity in zebrafish (Danio rerio).* J Hazard Mater, 2014. **277**: p. 134-40.

71. Ma, H., et al., *Impact of solar UV radiation on toxicity of ZnO nanoparticles through photocatalytic reactive oxygen species (ROS) generation and photo-induced dissolution.* Environ Pollut, 2014. **193**: p. 165-172.
72. Sirelkhatim, A., et al., *Review on Zinc Oxide Nanoparticles: Antibacterial Activity and Toxicity Mechanism.* Nanomicro Lett, 2015. **7**(3): p. 219-242.
73. Jones, N., et al., *Antibacterial activity of ZnO nanoparticle suspensions on a broad spectrum of microorganisms.* FEMS Microbiol Lett, 2008. **279**(1): p. 71-6.
74. Seil, J.T. and T.J. Webster, *Antimicrobial applications of nanotechnology: methods and literature.* Int J Nanomedicine, 2012. **7**: p. 2767-81.
75. Barra Caracciolo, A., E. Topp, and P. Grenni, *Pharmaceuticals in the environment: biodegradation and effects on natural microbial communities. A review.* J Pharm Biomed Anal, 2015. **106**: p. 25-36.
76. Deda, D.K., et al., *Porphyrin Derivative Nanoformulations for Therapy and Antiparasitic Agents.* Molecules, 2020. **25**(9).
77. Imran, M., et al., *Emerging Applications of Porphyrins and Metalloporphyrins in Biomedicine and Diagnostic Magnetic Resonance Imaging.* Biosensors (Basel), 2018. **8**(4).
78. Huang, X. and J.T. Groves, *Oxygen Activation and Radical Transformations in Heme Proteins and Metalloporphyrins.* Chem Rev, 2018. **118**(5): p. 2491-2553.
79. Stawski, W., M. Kijewska, and M. Pawlicki, *Multi-Cation Coordination in Porphyrinoids.* Chem Asian J, 2020. **15**(1): p. 8-20.
80. Taniguchi, M. and J.S. Lindsey, *Synthetic Chlorins, Possible Surrogates for Chlorophylls, Prepared by Derivatization of Porphyrins.* Chem Rev, 2017. **117**(2): p. 344-535.
81. Kou, J.Y.; Dou, D.; Yang, L.M. (2017) Porphyrin photosensitizers in photodynamic therapy and its applications. *Oncotarget 8*, 81591–81603..
82. Tian, J., et al., *Fluorescence quenching and spectrophotometric methods for the determination of daunorubicin with meso-tera (4-sulphophenyl) porphyrin as probe.* Spectrochim Acta A Mol Biomol Spectrosc, 2014. **120**: p. 7-13.
83. Esteves, C.H.A., et al., *New composite porphyrin-conductive polymer gas sensors for application in electronic noses.* Sensors and Actuators B: Chemical, 2014. **193**: p. 136-141.
84. Zhang, W., W. Lai, and R. Cao, *Energy-Related Small Molecule Activation Reactions: Oxygen Reduction and Hydrogen and Oxygen Evolution Reactions Catalyzed by Porphyrin- and Corrole-Based Systems.* Chem Rev, 2017. **117**(4): p. 3717-3797.
85. Tsolekile, N., S. Nelana, and O.S. Oluwafemi, *Porphyrin as Diagnostic and Therapeutic Agent.* Molecules, 2019. **24**(14).
86. Frochot, C. and S. Mordon, *Update of the situation of clinical photodynamic therapy in Europe in the 2003–2018 period.* Journal of Porphyrins and Phthalocyanines, 2019. **23**(04n05): p. 347-357.
87. Fuhrmann, G., et al., *Active loading into extracellular vesicles significantly improves the cellular uptake and photodynamic effect of porphyrins.* J Control Release, 2015. **205**: p. 35-44.
88. Svenson, S. and D.A. Tomalia, *Dendrimers in biomedical applications--reflections on the field.* Adv Drug Deliv Rev, 2005. **57**(15): p. 2106-29.

89. Cheng, L., et al., *Functional nanomaterials for phototherapies of cancer.* Chem Rev, 2014. **114**(21): p. 10869-939.
90. *<ghoroghchian2005.pdf>.*
91. Lovell, J.F., et al., *Porphysome nanovesicles generated by porphyrin bilayers for use as multimodal biophotonic contrast agents.* Nat Mater, 2011. **10**(4): p. 324-32.
92. Huynh, E. and G. Zheng, *Porphysome nanotechnology: A paradigm shift in lipid-based supramolecular structures.* Nano Today, 2014. **9**(2): p. 212-222.
93. Nguyen KT, West JL.(2002) Photopolymerizable hydrogels for tissue engineering applications. Biomaterials 23:4307–14.
94. Van Vlierberghe, S., P. Dubruel, and E. Schacht, *Biopolymer-based hydrogels as scaffolds for tissue engineering applications: a review.* Biomacromolecules, 2011. **12**(5): p. 1387-408.
95. Brandl, F., et al., *Hydrogel-based drug delivery systems: comparison of drug diffusivity and release kinetics.* J Control Release, 2010. **142**(2): p. 221-8.
96. Hah, H.J., et al., *Methylene blue-conjugated hydrogel nanoparticles and tumor-cell targeted photodynamic therapy.* Macromol Biosci, 2011. **11**(1): p. 90-9.
97. Fallows, S.J., et al., *Electrically-responsive anti-adherent hydrogels for photodynamic antimicrobial chemotherapy.* J Photochem Photobiol B, 2012. **114**: p. 61-72.
98. Wu, F., et al., *Facile synthesis of N-rich carbon quantum dots from porphyrins as efficient probes for bioimaging and biosensing in living cells.* Int J Nanomedicine, 2017. **12**: p. 7375-7391.
99. Liu, Y., et al., *Optical behaviors of ZnO-porphyrin conjugates and their potential applications for cancer treatment.* Applied Physics Letters, 2008. **92**(14).
100. Zhang, Y., et al., *Phototoxicity of Zinc Oxide Nanoparticle Conjugatesin Human Ovarian Cancer NIH: OVCAR-3 Cells.* Journal of Biomedical Nanotechnology, 2008. **4**(4): p. 432-438.
101. Bihari, P., et al., *Optimized dispersion of nanoparticles for biological in vitro and in vivo studies.* Part Fibre Toxicol, 2008. **5**: p. 14.
102. Suntako, R., (2015) Effect of zinc oxide nanoparticles synthesized by a precipitation method on mechanical and morphological properties of the CR foam. Bulletin of Materials Science, 38 (4), 1033-1038..
103. Bacaksiz, E., et al., *The effects of zinc nitrate, zinc acetate and zinc chloride precursors on investigation of structural and optical properties of ZnO thin films.* Journal of Alloys and Compounds, 2008. **466**(1-2): p. 447-450.
104. Ahirwar, S., S. Mallick, and D. Bahadur, *Electrochemical Method To Prepare Graphene Quantum Dots and Graphene Oxide Quantum Dots.* ACS Omega, 2017. **2**(11): p. 8343-8353.
105. Visali, P. and R. Bhuvaneswari, *Photoluminescence and enhanced photocatalytic activity of ZnO nanoparticles through incorporation of metal dopants Al and Ca.* Optik, 2020. **202**.
106. Jeong, E.-Y., et al., *Synthesis and catalytic behavior of tetrakis(4-carboxyphenyl) porphyrin-periodic mesoporous organosilica.* Journal of Materials Chemistry, 2010. **20**(48).

107. Hiromitsu, I., et al., *Luminescence of tetraphenylporphyrin by an energy transfer from photoexcited ZnO nanoparticle.* Chemical Physics Letters, 2011. **501**(4-6): p. 385-389.
108. Lagopati, N., et al., *Photo-induced treatment of breast epithelial cancer cells using nanostructured titanium dioxide solution.* Journal of Photochemistry and Photobiology A: Chemistry, 2010. **214**(2-3): p. 215-223.
109. Dager, A., et al., *Synthesis and characterization of Mono-disperse Carbon Quantum Dots from Fennel Seeds: Photoluminescence analysis using Machine Learning.* Sci Rep, 2019. **9**(1): p. 14004.
110. Suzuki, K., et al., *Design of Carbon Dots Photoluminescence through Organo-Functional Silane Grafting for Solid-State Emitting Devices.* Sci Rep, 2017. **7**(1): p. 5469.
111. Mroz, P., et al., *Cell death pathways in photodynamic therapy of cancer.* Cancers (Basel), 2011. **3**(2): p. 2516-39.

112. Papadimitriou, D., (2003) Optical Spectroscopy: Methods of Optical and Structual Characterization, Athens, 317-322

113. Kulkarni, S. K., (2015) Nanotechnology: principles and practices, 3rd edition, 171-172. ISBN-13: 978-3319091709

114. Bouroushian, M., (2005) Solid State Chemistry, Athens, National Technical University of Athens (NKUA) (In Greek)

115. Ochsenkuhn, M., (2020) XRD, Class materials for the MSc Materials Science and Engineering, School of Chemical Engineering, National Technical University of Athens, Greece

116. Reusch, W., UV-Visible Spectroscopy, (2013) Retrieved from https://www2.chemistry.msu.edu/faculty/reusch/virttxtjml/spectrpy/uvvis/uvspec.htm#uv1

117. Theophanides, T., (1978) Infrared and Raman spectroscopy of biological molecules. NATO Advanced Study Institute. D Reidel Publishing Co, Dordrecht,

118. Theophanides, T., (2004) Introduction to Infrared Spectroscopy. Infrared Spectroscopy. Materials Science, the Sciences Series. ISBN: 978-0-470-85428-0, 5-8